


**Please cite the Published Version**

Letona-Elizburu, A, Enterría, M, Aziz, A , Villar-Rodil, S, Paredes, JI, Carrasco, J and Ortiz-Vitoriano, N (2024) Biomimetic nucleotide-graphene hybrids for electrocatalytic oxygen conversion: quantifying biomolecule mass loading. *Sustainable Materials and Technologies*, 39. e00835  
ISSN 2214-9937

**DOI:** <https://doi.org/10.1016/j.susmat.2024.e00835>

**Publisher:** Elsevier

**Version:** Published Version

**Downloaded from:** <https://e-space.mmu.ac.uk/634855/>

**Usage rights:**  [Creative Commons: Attribution-Noncommercial-No Derivative Works 4.0](https://creativecommons.org/licenses/by-nc-nd/4.0/)

**Additional Information:** This is an open access article which first appeared in *Sustainable Materials and Technologies*

**Data Access Statement:** Data will be made available on request.

**Enquiries:**

If you have questions about this document, contact [openresearch@mmu.ac.uk](mailto:openresearch@mmu.ac.uk). Please include the URL of the record in e-space. If you believe that your, or a third party's rights have been compromised through this document please see our Take Down policy (available from <https://www.mmu.ac.uk/library/using-the-library/policies-and-guidelines>)



## Biomimetic nucleotide-graphene hybrids for electrocatalytic oxygen conversion: Quantifying biomolecule mass loading

A. Letona-Elizburu<sup>a,b</sup>, M. Enterría<sup>a,\*</sup>, A. Aziz<sup>a</sup>, S. Villar-Rodil<sup>c</sup>, J.I. Paredes<sup>c</sup>, J. Carrasco<sup>a,d</sup>, N. Ortiz-Vitoriano<sup>a,d,\*</sup>

<sup>a</sup> Center for Cooperative Research on Alternative Energies (CIC energiGUNE), Basque Research and Technology Alliance (BRTA), Alava Technology Park, Albert Einstein 48, 01510, Spain

<sup>b</sup> University of the Basque Country (UPV / EHU), Barrio Sarriena, s/n, Leioa 48940, Spain

<sup>c</sup> Instituto de Ciencia y Tecnología del Carbono INCAR-CSIC, C/Francisco Pintado Fe 26, Oviedo 33011, Spain

<sup>d</sup> Ikerbasque, Basque Foundation for Science, Plaza Euskadi 5, Bilbao 48009, Spain

### ARTICLE INFO

#### Keywords:

Metal-free electrocatalysts

Loading

Bioinspired graphene based electrocatalysts

Gas conversion technologies

ORR/OER reactions

Nucleotides

### ABSTRACT

Metal-free electrocatalysts for the electrochemical conversion of gases constitute an important asset for a sustainable energy transition. Nucleotides act as redox mediators in the electron transport chain to reduce oxygen in cellular respiration. The biomimicry of such an efficient natural mechanism could be utilized to address the challenges associated with electrochemical gas conversion technologies, such as sluggish kinetics and high overpotentials. Multiple descriptors are generally reported to benchmark the activity of electrocatalysts where the turnover frequency (TOF) is claimed to be the most accurate criterion. Here, a library of graphene nanosheets-nucleotide hybrid materials was prepared, and the electrocatalytic performance towards ORR/OER reactions of a graphene-flavin mononucleotide hybrid was evaluated by rotating disc electrode experiments and TOF estimation. The determination of catalyst loading and dispersion is especially relevant when assessing the intrinsic activity of a catalyst and, therefore, the amount of nucleotide electrocatalyst loaded into the graphene support was thoroughly quantified by a combination of characterization techniques. Density functional theory calculations supported the observed experimental trends, both on the adsorption rate of a given nucleotide on graphene and the catalytic activity of a specific hybrid material. This work constitutes an avenue to predict nature-mimicking electrocatalysts for efficient energy storage.

### 1. Introduction

Global warming and the energy crisis require the search for new technologies to support the transition from fossil fuels to sustainable and environmentally friendly resources [1–3]. Renewable energy sources such as wind and solar are increasingly being adopted; however, their intermittent nature makes the development of long-term storage solutions critical [2]. In this context, the combination of electrolyzers [1] – oxygen evolution and hydrogen evolution reactions (OER, HER) – with fuel cells – oxygen reduction and hydrogen oxidation (ORR, HOR) – to create a regenerative fuel cell for storing electrochemical energy is an attractive approach [1–6]. Another promising option for high-capacity energy storage are metal-air batteries, which operate through the electrochemical conversion of gases, involving the ORR during discharge

and the reversible oxidation of oxygen (OER) during charge [7–10].

The electrochemical reduction/oxidation of gases is, therefore, a very interesting approach to bridge the gap between environmental remediation and future energy supply [11–20]. However, all these reactions present high overpotentials and low energy efficiencies which have led to extensive efforts devoted to the development of efficient electrocatalysts [21–27]. While precious metals and metal transition oxides have been extensively studied for various reactions [28–38], their limited availability and high-cost highlight the need for developing metal-free bifunctional materials [5,32,39–41].

Proteins, metal complexes or ribozymes – small biomolecules found in living organisms – are considered potential alternative electrocatalysts capable of catalyzing both oxidation and reduction reactions [42–45]. For instance, nucleotides are metal-free, simple and relatively

\* Corresponding authors at: Center for Cooperative Research on Alternative Energies (CIC energiGUNE), Basque Research and Technology Alliance (BRTA), Alava Technology Park, Albert Einstein 48, 01510, Spain.

E-mail addresses: [menterria@cicenergigune.com](mailto:menterria@cicenergigune.com) (M. Enterría), [nortiz@cicenergigune.com](mailto:nortiz@cicenergigune.com) (N. Ortiz-Vitoriano).

<https://doi.org/10.1016/j.susmat.2024.e00835>

Received 31 October 2023; Received in revised form 18 January 2024; Accepted 19 January 2024

Available online 22 January 2024

2214-9937/© 2024 The Author(s). Published by Elsevier B.V. This is an open access article under the CC BY-NC-ND license (<http://creativecommons.org/licenses/by-nc-nd/4.0/>).

cheap molecules which participate as redox enzyme cofactors for oxygen reduction in cellular respiration [46–48]. Such complex and efficient multiphase chemistry in metabolic pathways is very similar to that limiting the performance of fuel cells or metal-air batteries. However, nucleotides lack electronic conductivity, necessitating their incorporation into conductive materials for ORR and OER. In this context, carbon materials have been extensively studied as supports and conductive agents [33,42,49–58]. Specifically, graphene's exceptional electrical conductivity and 2D accessible surface area make it an excellent support for adsorbing and maximizing the electrocatalytic activity of biological catalysts [25,52,59]. Particularly, the conjugated nucleobase in the nucleotides can strongly attach via  $\pi$ - $\pi$  stacking with the electronically conjugated structure of graphene, producing a synergy between the electrical conductivity of the carbon material and the catalytic effect of the nucleotide [60–62].

High-throughput experimental and computational studies have focused on screening the electrocatalytic activity of nitrogen heterocyclic molecules, analogous to nucleotides, grafted onto different carbon supports for ORR, showcasing promising results [5,41,63]. However, while these nitrogen heterocyclic molecules hold significant potential as electrocatalysts for energy conversion and storage, the electrocatalytic activity of nucleotides in this specific context remains largely unexplored [38,64].

In this work, we prepared a small library of nucleotide/graphene hybrids through a straightforward liquid adsorption process in low-oxidized graphene nanosheets obtained by electrochemical exfoliation. These six nucleotides were chosen based on the structure of the nucleobase (different aromatic rings and functional groups, to explore potentially different behaviors) as their redox properties generally derive from the molecular structure of their nucleobase [47]. Herein, we determined the quantification of loading and dispersion of such hybrid metal-free catalysts through TGA, UV-vis absorption spectroscopy, energy dispersive X-ray microscopy and X-ray photoelectron spectroscopy (XPS) which is an unexplored field. In addition, we further validated the experimental results by modeling the adsorption energies of the nucleotides on the graphene surface.

Regarding the catalytic capacity of nucleotides, we hypothesized that the presence of nucleotides adsorbed on graphene might improve their oxygen kinetics. First, graphene provides a conductive support for the electrons which are readily shuttled to the redox-active centers; second, the high oxygen binding affinity of these nucleotides could facilitate the diffusion of oxygen through the electrode. Therefore, as illustrated in Fig. 1, nucleotides are expected to act as well-dispersed

oxygen binding species in their hybrids with graphene, so that electrocatalytic active centers would be present in most of the carbon support, thus improving oxygen diffusion and reaction kinetics.

If the hypothesis proposed in Fig. 1 is confirmed, it would open the path towards the development of innovative metal-free bio-based bifunctional catalysts with enhanced ORR and OER kinetics for a wide range of devices such as electrolyzers, metal-air batteries and beyond.

## 2. Experimental and computational methods

### 2.1. Chemicals

Xanthosine-5'-monophosphate (XMP, Cayman Chemical), inosine-5'-monophosphate disodium salt hydrate (IMP, Thermoscientific, crystalline powder), guanosine-5'-monophosphate disodium salt hydrate (GMP, Sigma Aldrich, from yeast  $\geq 99.0\%$ ), thymidine-5'-monophosphate disodium salt (TMP, Thermoscientific, powder), cytidine-5'-monophosphate disodium salt (CMP, Thermoscientific, 99 + % crystalline powder), riboflavin-5'-phosphate sodium salt dihydrate (FMN, Thermoscientific), sodium sulfate ( $\text{Na}_2\text{SO}_4$ , Sigma Aldrich,  $\geq 99.0\%$  anhydrous), sodium chloride (NaCl, Scharlau, reagent grade, ACS), 2-propanol (or isopropanol, IPA, Thermoscientific, GC Grade, 99.7 + %), Nafion 117 containing solution (Sigma Aldrich, ~5% in a mixture of lower aliphatic alcohols and water).

### 2.2. Anodic exfoliation of graphite: preparation and physicochemical characterization of low-oxidized graphene nanosheets

A graphite foil (25x45x1 mm, from Mersen PAPYEX® I980) was anodically exfoliated using a platinum foil (25x25x0.025 mm<sup>3</sup>, purity 99.95%, from GoodFellow) as the cathode. The two electrodes were immersed into an aqueous 0.1 M  $\text{Na}_2\text{SO}_4$  solution at a distance of 1 cm from each other. The sulfate anion is known to intercalate and expand the interlayer space of graphite under anodic conditions [65]. Sodium sulfate was chosen for this study because it is a mild and innocuous compound, making it safer to handle compared to strong acids (e.g.,  $\text{H}_2\text{SO}_4$ ) that are also used in the preparation of graphene by (electro) chemical exfoliation of graphite. Furthermore, sodium sulfate has been reported to yield high-quality graphene nanosheets with low to moderate levels of oxidation [66]. The electrodes were connected to a Keysight E3633A power supply and a positive voltage of 10 V was applied to the graphite foil electrode for 1 h. Afterwards, the electrolyte was removed by filtration and the resulting highly expanded graphite

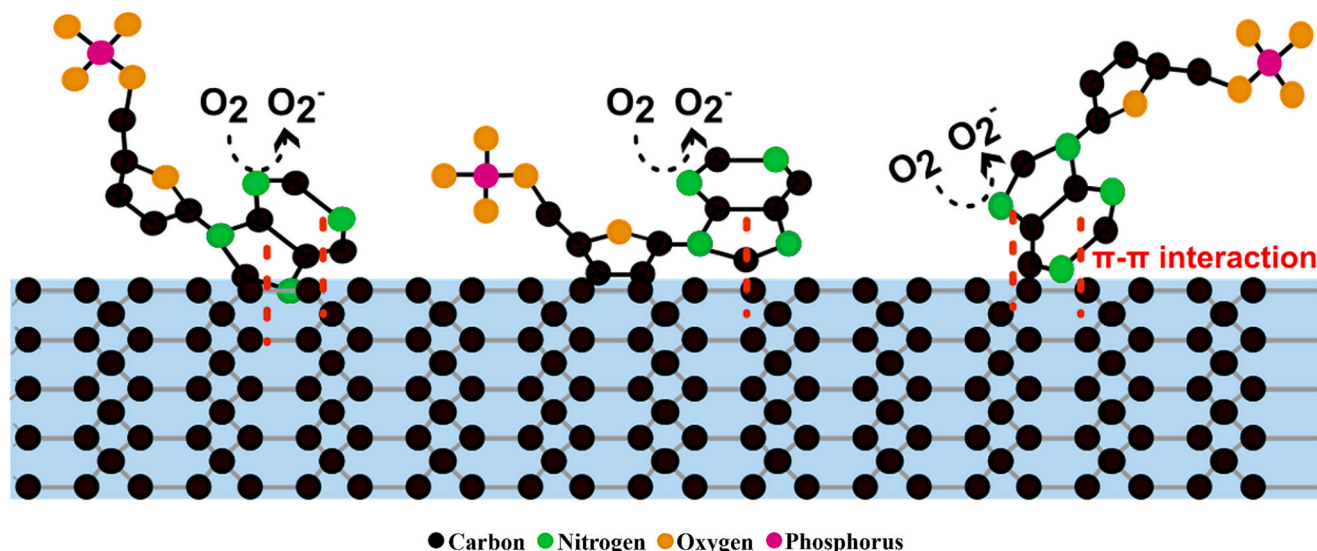


Fig. 1. Hypothesis on how nucleotides adsorbed on graphene by  $\pi$ - $\pi$  interactions would act as electrocatalytic active centers for ORR and OER.

particles were washed with 1 L of deionized water. The obtained powder was further washed to remove the electrolyte excess by recovering the material from the filter with an additional 200 mL of deionized water, stirring for 2 h and filtering. Then, 200 mL of an isopropanol/water (IPA/H<sub>2</sub>O) mixture (35/65 v/v %, pH = 7.29) was added to the filtered material and sonicated in a J.P.Selecta Ultrasons system (40 kHz; power: 30 W L<sup>-1</sup>) for 3 h to complete delamination of the expanded graphite into individual graphene nanosheets. The dispersion of graphene nanosheets in IPA/H<sub>2</sub>O was subjected to low-speed centrifugation (2000 g, 20 min; Sorvall Legend X1 centrifuge, Thermo Scientific) to eliminate the non-fully exfoliated graphite. The graphite sediment was discarded, and the supernatant enriched in graphene nanosheets was kept. The concentration of the graphene dispersion was determined by UV–vis absorption spectroscopy (VARIAN Cary 5000) through Lambert-Beer's law (Fig. S1a) and diluting by a factor of 451. The absorbance was measured at a wavelength of 660 nm, using a previously estimated extinction coefficient of  $\epsilon_{660} = 2440 \text{ mL mg}^{-1} \text{ m}^{-1}$  [67]. The concentration of the graphene dispersion was adjusted to 2 mg mL<sup>-1</sup> by centrifugation of the dispersion at 25000 g for 20 min (Biocen 22 centrifuge, Ortoalesa) to sediment the graphene and adding a suitable amount of IPA/H<sub>2</sub>O solvent.

The morphology of drop-cast graphene layers was characterized using atomic force microscopy (AFM). To this end, the obtained dispersions were diluted by a factor of 50 and the diluted dispersion was sonicated for 15 min. 10  $\mu\text{L}$  of diluted dispersion was deposited on a mica substrate and placed for 2 h in an oven at 60 °C. Subsequently, an additional 10  $\mu\text{L}$  was added and left overnight at 60 °C. To complete drying, the mica was placed in a vacuum oven at 120 °C for 72 h. AFM images were recorded in the tapping mode of operation with an Agilent 5500 AFM apparatus. Non-reflective silicon cantilevers (APP Nano) with nominal spring constant about 40 N/m and resonant frequency of 295 kHz were used.

For preparing graphene aerogel powders, part of the graphene dispersion was centrifuged at high speed (25,000 g, 20 min) to sediment the graphene fraction and to redisperse in neat water. The aqueous dispersions were frozen at -75 °C in an ultra-freezer and subsequently

freeze-dried in a Telstar LyoQuest equipment at -80 °C for 72 h (aqueous dispersions of graphene were prepared instead of those with IPA/H<sub>2</sub>O as alcohols can damage the freeze-dryer). The structural order of the graphene nanosheets comprising the aerogel was studied by Raman spectroscopy using a Renishaw spectrometer (Nanionics Multi-view 2000) operating with an excitation wavelength of 532 nm, focused with a 50X long working distance objective. The spectra were obtained by performing 10 acquisitions with 10 s of exposure time of the laser beam to the sample. The oxidation degree of the graphene nanosheets was also studied from the aerogel powders by XPS on a SPECS spectrometer equipped with a Phoibos 100 hemispherical electron energy analyzer. The spectra were acquired at a pressure below 10<sup>-7</sup> Pa using a monochromatic Al K $\alpha$  X-ray source operated at a voltage of 14.00 KV and a power of 175 W. The spectra were acquired at a take-off angle of 90°. The photo-excited electrons were analyzed in constant pass energy mode, using a pass energy of 50 eV. The use of bulky graphene aerogels instead of dispersed/deposited specimens for the Raman and XPS characterization was preferred as both are surface techniques. An insufficient thickness of the samples might lead to inaccurate results due to the interference of the support. The aerogel powders were processed using a die by pressing them at 0.5 Ton for 1 min prior to the analysis.

### 2.3. Preparation of nucleotide/graphene nanosheet hybrids

Fig. 2 shows the chemical structure and acronyms of the nucleotides selected for the preparation of hybrids with graphene. Nucleotides are comprised of a phosphate group, a pentose sugar and a nitrogenous heterocyclic nucleobase, which in turn can be composed of a one-ring pyrimidine or a two-ring purine aromatic moiety). The chemical structure for each nucleotide is presented considering the pH (7.29) of the IPA/H<sub>2</sub>O solvent used to disperse the graphene nanosheets. The phosphate anions in the sodium nucleotide salts possess pK<sub>a</sub> values around 3.9 and 6.1 [68], and therefore they are deprotonated at neutral pH. Also, the pK<sub>a</sub> of the functional groups in the different nucleobases, except xanthine, lie above the solvent pH, so the nucleobases themselves will be electrically neutral. For xanthosine monophosphate (XMP), one

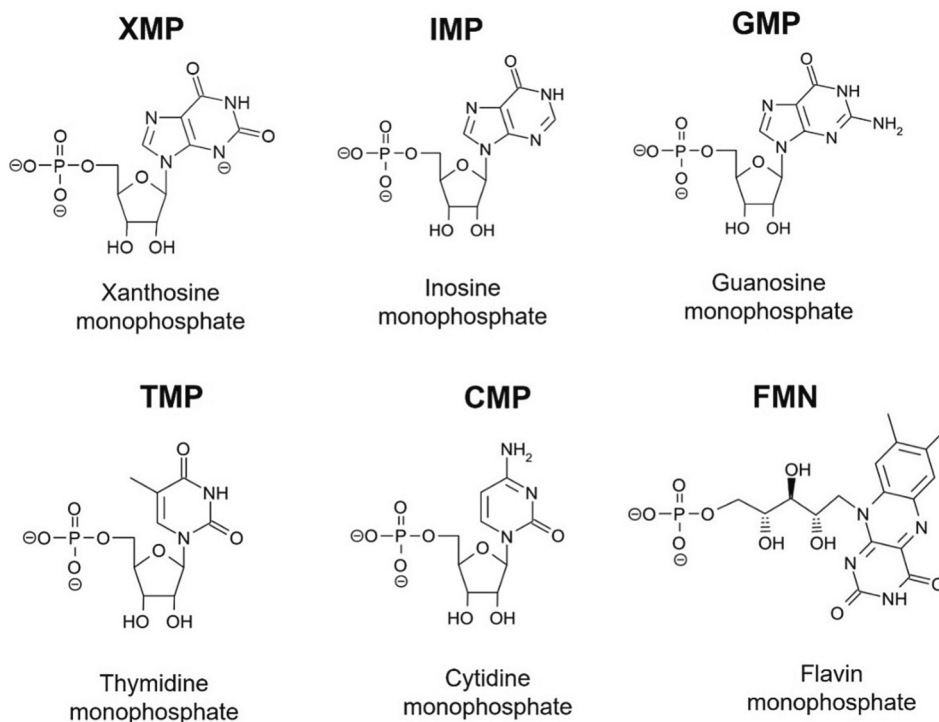


**Fig. 2.** Molecular structure of the different nucleotides used in this work to prepare the nucleotide/graphene hybrid materials at pH 7.29. The nomenclature used to reference each molecule is also indicated.



of the -NH groups in the xanthine nucleobase presents a  $pK_a$  value of 6.4 [69]. This group will therefore be deprotonated at the solvent pH, lending the molecule an additional negative charge. All the nucleotides of Fig. 2 were adsorbed onto the anodically exfoliated graphene nanosheets following the procedure schematically depicted in Fig. S2.

Concentrated solutions of adsorbate ( $5 \text{ mg mL}^{-1}$  or  $0.01 \text{ mol L}^{-1}$ ) were prepared by directly adding 20 mg of each mononucleotide salt on 4 mL of a  $2 \text{ mg mL}^{-1}$  graphene dispersion. The mixture was bath-sonicated for 20 min and left in a roll stirrer for 24 h at 60 rpm to ensure the physical adsorption of the nucleotide onto the graphene nanosheets. The dispersion was then submitted to high-speed centrifugation ( $25,000 \text{ g}$ ) for 20 min to separate the nucleotide/graphene hybrid from the nucleotide solution by sedimentation: (1) the supernatant (referred to as SP1) was collected and (2) the sediment was redispersed in 4 mL of fresh IPA/H<sub>2</sub>O to wash the hybrid material and remove free nucleotide molecules remaining in the small volume of solvent collected with the sediment. To this end, the redispersed sediment was bath-sonicated for 20 min, roll-stirred for 30 min at 60 rpm, and then recovered by centrifugation ( $25,000 \text{ g}$  for 20 min): (1) the resulting supernatant (referred to as SP2) was collected and (2) the sediment containing the nucleotide/graphene hybrid was redispersed in neat water and freeze-dried under the same conditions as those used for graphene dispersions in Section 2.2. The hybrid materials were denoted as "HX", where X stands for the nucleotide acronym as defined in Fig. 2. For instance, XMP is the pure xanthosine monophosphate salt and HXMP is the xanthosine monophosphate/graphene hybrid material.

#### 2.4. Quantification of the nucleotide loading in the hybrid material

Besides intrinsic activity, loading and dispersion are the most important parameters affecting the performance of a given (electro) catalyst [70,71]. The study of these parameters is well established for metal-based catalysts, where thermogravimetric analysis (TGA), inductively coupled plasma (ICP), or hydrogen chemisorption are extensively used [71–73]. However, the determination of loading and dispersion of metal-free catalysts is still underexplored, necessitating the development of suitable and accurate techniques prior to conducting electrochemical performance tests. This challenge becomes particularly pronounced when working with graphene, as its low density and poor dispersibility in aqueous solvents make it inherently difficult to process.

The amount of mononucleotide salt adsorbed onto the graphene nanosheets was calculated indirectly by UV–vis absorption spectroscopy from Eq. (1).

$$\% \text{Adsorbed nucleotide} = \frac{[C_0] \cdot V_t - [SP1] \cdot V_s - [SP2] \cdot V_s}{M} \cdot 100 \quad (1)$$

where  $[C_0]$  is the concentration of the nucleotide salt in the initial solution,  $V_t$  is the total volume of the initial dispersion,  $[SP1]$  is the concentration of the nucleotide on the supernatant after the adsorption,  $V_s$  is the supernatant volume, and  $[SP2]$  is the concentration of the nucleotide in the supernatant resulting from washing the hybrid material.  $[SP2]$  considers both the nucleotide molecules desorbed from the hybrid and those which were not adsorbed in the graphene nanosheets but were collected with the sediment in a small volume of solvent.  $[SP1]$  and  $[SP2]$  were calculated with the assistance of calibration curves plotting absorbance vs. nucleotide concentration, which had been previously determined. To this end,  $1 \text{ mg mL}^{-1}$  stock solutions of nucleotide salts in IPA/H<sub>2</sub>O (35:65) solvent were first prepared. Diluted solutions ranging from  $5 \times 10^{-3}$  to  $7 \times 10^{-2} \text{ mg mL}^{-1}$  were then obtained from the stock solution and measured by UV–vis absorption spectroscopy at a wavelength characteristic of each nucleotide (Fig. S1b and S1c:  $\lambda_{\text{max, AMP}} = 259 \text{ nm}$ ,  $\lambda_{\text{max, CMP}} = 272 \text{ nm}$ ,  $\lambda_{\text{max, GMP}} = 254 \text{ nm}$ ,  $\lambda_{\text{max, IMP}} = 250 \text{ nm}$ ,  $\lambda_{\text{max, FMN}} = 448 \text{ nm}$ ,  $\lambda_{\text{max, TMP}} = 267 \text{ nm}$ ,  $\lambda_{\text{max, XMP}} = 278 \text{ nm}$ ), from which the calibration plots were derived (Fig. S3).

Complementary to the UV–vis absorption spectroscopy technique,

the amount of adsorbed nucleotide on the graphene support was estimated using TGA. In this case, the freeze-dried nucleotide/graphene hybrid in aerogel powder form (Fig. S2) was directly analyzed on a NETZSCH STA 449 F3 Jupiter equipment, in argon atmosphere with a heating ramp of  $10 \text{ }^\circ\text{C min}^{-1}$  up to  $1000 \text{ }^\circ\text{C}$ . A 1 h isothermal step at  $100 \text{ }^\circ\text{C}$  on the TGA apparatus was included to completely remove water from the hygroscopic nucleotide salts. The amount of nucleotide adsorbed onto the graphene surface was estimated using Eq. (2),

$$\%M(\text{Nucleotide in the hybrid}) = \frac{\%R(\text{hybrid}) - \%R(\text{graphene})}{\%R(\text{nucleotide}) - \%R(\text{graphene})} \times 100 \quad (2)$$

where %R is the mass percentage of the residue remaining in each sample after the heat treatment at  $1000 \text{ }^\circ\text{C}$ . This equation was rationalized following the assumptions included in the Supporting Information and considering that:

- 1) The decomposition of the ribose/nucleobase in the nucleotide upon heat treatment results in the release of H<sub>2</sub>O, CO<sub>2</sub>, HCNO, and NH<sub>3</sub>. However, the phosphate moiety remains as refractory oxides, along with the graphene support [38,74–77]. Hence, when determining the quantity of nucleotide, it is necessary to consider the residues left behind by the two phases separately (graphene and nucleotide salt), as well as the residue left by the hybrid material.
- 2) The amount of residue left behind by both stand-alone components (i.e., graphene and nucleotides separately) is the same as that of their counterparts in the hybrid material.

A third quantification of the amount of nucleotide adsorbed in the nucleotide/graphene hybrids was conducted by XPS on a SPECS spectrometer equipped with a Phoibos 100 hemispherical electron energy analyzer. Different pellets were prepared from hybrid aerogel powders using a die and pressing them at 0.5 Ton for 1 min. The spectra were acquired at a pressure below  $10^{-7} \text{ Pa}$  using a monochromatic Al K $\alpha$  X-ray source operated at a voltage of 14.00 kV and a power of 175 W. The spectra were acquired at a take-off angle of  $90^\circ$ . The photo-excited electrons were analyzed in constant pass energy mode, using a pass energy of 50 eV.

#### 2.5. Estimation of nucleotide solubility in IPA/H<sub>2</sub>O solvent

The solubility of each nucleotide salt was estimated by preparing supersaturated solutions of the different mononucleotide sodium salts in the 35/65 v/v% IPA/H<sub>2</sub>O solvent. The solutions were centrifuged at  $10000 \text{ g}$  for 20 min to remove the non-dissolved (dispersed) salt and the concentration of the supernatant was measured by UV–vis absorption spectroscopy using the calibration curves displayed in Fig. S3.

#### 2.6. Dispersion of the nucleotides in the hybrid material

The dispersion of the nucleotides on the surface of the graphene support was studied by Scanning Electron Microscopy-Energy Dispersive X-Ray spectroscopy (SEM-EDX) using a FEI Quanta 250 microscope equipped with an ADC1 detector operating at 10.00 kV, spot size set at 3.5 and a dwell of 1000  $\mu\text{s}$ . The EDX mapping images were acquired for phosphorous and nitrogen atoms at a magnification of  $\times 50$ .

#### 2.7. Assessment of the ORR/OER electrocatalytic performance of a hybrid material

The electrocatalytic activity towards ORR/OER reactions of HFMN hybrid material was studied to explore the potential of nucleotides in energy conversion technologies. Graphene without any nucleotide adsorbed on its surface was also tested for comparison. The tests were conducted on a three-electrode configuration cell, using a glassy carbon

Rotating Disk Electrode (RDE, Blue Rev. from BioLogic) coupled with a VMP3 potentiostat (BioLogic). A Pt wire was utilized as a counter electrode and a Hg/HgO (NaOH 1 M) reference electrode. For the experiments, an alkaline electrolyte (0.1 M KOH) was selected, aligning with previous studies in the literature. This choice allows for a standard benchmark to assess the performance of the materials under investigation.

The working electrodes were manufactured by drop casting an ink based on either the graphene or HF MN dispersions. 40  $\mu\text{L}$  of Nafion 117 were added to 1 mL of 4 mg  $\text{mL}^{-1}$  dispersions to fix a graphene (or hybrid)/Nafion weight ratio of 2:1. The mixture was stirred at a rate of 60 rpm for 20 min. Subsequently, a 10  $\mu\text{L}$  aliquot of the prepared ink was cast onto the glassy carbon tip to achieve a mass loading of 0.102 mg  $\text{cm}^{-2}$ .

Linear sweep voltammetry (LSV) curves were registered using a rotation speed of 1600 rpm. For ORR, the potential was linearly scanned from 0.05 to -0.65 V vs. reference electrode, with a scan rate of 10  $\text{mV s}^{-1}$  in the presence of continuous  $\text{O}_2$  flow over the solution; for OER, the potential was linearly scanned from 0.0 to +0.90 V vs. reference electrode, with a scan rate of 10  $\text{mV s}^{-1}$  in presence of continuous  $\text{N}_2$  flow over the solution. For ORR measurement, a background in the same conditions and an inert  $\text{N}_2$  atmosphere was collected and subtracted during data processing to correct capacitive effects. The potentials were converted to reversible hydrogen electrode (RHE) to take into consideration the effect of pH, and corrected for the Ohmic drop, between the reference and the working electrode, by applying the following equations:

$$E_{\text{RHE}} = E_{\text{exp}} + \text{pH} \cdot 2.303 \cdot \frac{RT}{F} + E_{\text{Hg/HgO}} \quad (3)$$

$$E_{\text{corr}} = E_{\text{RHE}} - i \cdot R_u \quad (4)$$

where  $E_{\text{RHE}}$  is the potential referred to the RHE,  $E_{\text{exp}}$  is the experimental potential recorded by the equipment, pH is that of the electrolyte solution (0.1 M KOH, pH 13), R is the universal gas constant (8.314  $\text{J mol}^{-1} \text{K}^{-1}$ ), F is the Faraday constant (96,485  $\text{C mol}^{-1}$ ), T is the temperature of the experiment ( $\approx 295.13 \text{ K}$ ),  $E_{\text{Hg/HgO}}$  is the reference potential vs. the standard hydrogen electrode (SHE) of the reference electrode (+143 mV vs. SHE),  $E_{\text{corr}}$  is the final potential vs. RHE corrected for the Ohmic drop,  $i$  is the current measured by the potentiostat, and  $R_u$  is solution ohmic resistance ( $\approx 60 \Omega$ ) previously determined by electrochemical impedance spectroscopy (EIS).

Regarding electrochemical performance, some activity descriptors are used in literature to benchmark the performance of a catalyst, notably the onset potential ( $E_{\text{onset}}$ ) and Tafel slope.  $E_{\text{onset}}$  is the potential value at which the studied reaction occurs, and the target product is formed at a given electrode and defined conditions [78]. The difference between this potential value and thermodynamic potential ( $E_0$ ) is crucial for determining the efficiency of an electrochemical system and is known as overpotential. Thus, the larger the overpotential (i.e. additional electromotive force required for the reaction to start) the less efficient the catalyst [79].  $E_{\text{onset}}$  can be calculated in two different ways: (1) by taking the value at the intersection point between two tangents in the current density vs. potential plot [80]; or (2) by registering the voltage at a given current density in which the studied reaction has already started. Here, the second approach was used and the voltages at a current density of -0.1  $\text{mA cm}^{-2}$  and +0.5  $\text{mA cm}^{-2}$  for ORR and OER reactions were considered, respectively. On the other hand, the Tafel equation (Eq. (5)) is a mathematical expression in electrochemical kinetics relating the rate, i.e. kinetic regime, of an electrochemical reaction to the overpotential [81–83]. From this equation, the so-called Tafel slope can be calculated, where a low value suggests a high catalytic activity and rapid reaction rate [84]. In this work the Tafel slope was calculated in the potential range of 0.76 and 0.81 V in ORR and 1.60 and 1.72 V in OER:

$$\eta = a + b \log(j) \quad (5)$$

where  $\eta$  is the overpotential,  $a$  is a constant,  $b$  is the Tafel slope and  $j$  is the current density ( $\text{mA cm}^{-2}$ ).

However,  $E_{\text{onset}}$  and the Tafel slope only provide an apparent evaluation of the activity of electrocatalysts; they assume that the amount of charge passed in a circuit is directly proportional to the amount of formed product, but they do not consider phenomena such as series resistance, electrolyte or electrode decomposition, secondary reactions, or capacitance [85]. In this sense, turnover frequency (TOF) has been claimed as a more suitable descriptor of the electrocatalytic activity as it measures the amount of product formed per unit time and the exact amount of catalyst used [79]. The lack of accurate ways of determining the amount of catalyst/number of active sites is the major bottleneck to use TOF as an activity descriptor for non-metallic catalyst. For TOF calculations, the number of moles of FMN nucleotide adsorbed in the HF MN hybrid material and deposited on the glassy carbon ( $n_{\text{FMN}}$ ) was calculated from:

$$n_{\text{FMN}} = \frac{m_{\text{HF MN}}}{V_{\text{ink}}} \cdot V_{\text{cast}} \cdot \frac{\% \text{FMN}_{\text{ads}}}{100} \cdot \frac{1}{M_{\text{FMN}}} \quad (6)$$

where  $m_{\text{HF MN}}$  is the mass of the hybrid,  $V_{\text{ink}}$  is the volume of ink,  $V_{\text{cast}}$  is the volume of ink cast,  $\% \text{FMN}_{\text{ads}}$  is the adsorbed percentage of FMN estimated in Table 2 and  $M_{\text{FMN}}$  is the molar mass of FMN.

The theoretical value of TOF for either the bare graphene and the FMN deposited in HF MN hybrid was calculated using:

$$\text{TOF} = \frac{i}{e^- \cdot F \cdot n_{\text{FMN}}} \quad (7)$$

where  $i$  is the measured current at  $E = 1.60 \text{ V}$ ,  $e^-$  is the number of electrons involved in OER reaction (4 electrons), F is the Faraday constant (96,485  $\text{C mol}^{-1}$ ) and  $n_{\text{FMN}}$  is the number of moles calculated in Eq. (6).

## 2.8. Computational models

### 2.8.1. Prediction of the adsorption energies of the different nucleotides on graphene surface

Density functional theory (DFT) calculations were performed using the periodic Vienna Ab initio Simulation Package (VASP) [86–89]. Geometry optimizations were performed at the  $\Gamma$ -point with a  $9 \times 9 \times 1$  supercell of the graphene unit-cell (space group P63/mmc [194]). The generalized gradient approximation (GGA) with the Perdew-Burke-Ernzerhof (PBE) functional was used [90] with the recommended pseudopotentials within the projector augmented wave formalism [91,92]. Energies and atomic forces were converged to within  $10^{-5} \text{ eV}$  and  $0.02 \text{ eV \AA}^{-1}$ , respectively using a  $\Gamma$ -centred  $3 \times 3 \times 1$   $k$ -mesh. The cut-off energy for the plane-wave expansion was set to 520 eV and vdW interactions were accounted for using the DFT-D3 method with Becke-Jonson damping [93,94]. This gave an optimized lattice parameter of 2.467  $\text{\AA}$ , in excellent agreement with the experimental value of graphite (2.464  $\text{\AA}$ ) [95]. To ensure charge neutrality the energies of the nucleotides were determined with the negatively charged oxygen ions on the phosphate group (Fig. 2) protonated.

Single-point solvation calculations were performed with VASPsol [96] and increasing the plane-wave expansion to 600 eV. As the contribution of the cavitation energy to the solvation energy has shown to be negligible, to avoid convergence issues the cavitation energy was neglected, and the surface tension parameter was set to 0 [96]. The size of the dielectric cavity is determined by a cut off electron density ( $n_c$ ) value, as well as the cavity width ( $\sigma$ ) [97]. Here we fixed  $\sigma$  to the default value of 0.6 and reduced  $n_c$  to  $1 \times 10^{-5} \text{ \AA}^{-3}$ , ensuring the implicit solvent formed at least 3  $\text{\AA}$  from the surface [98]. To model the 35–65 v/v% IPA/ $\text{H}_2\text{O}$  mixture used for the experimental work, the dielectric constant was set to 58 and the Debye length was set to 2.623  $\text{\AA}$ .

The adsorption energy ( $E_{ad}$ ) of each nucleotide was calculated from

$$E_{ad} = E_{total} - E_{clean} - E_{substrate} \quad (8)$$

where  $E_{total}$  is the total energy of the adsorbed nucleotide,  $E_{clean}$  is the energy of the clean graphene surface, and  $E_{substrate}$  is the energy of the isolated nucleotide. Each nucleotide was adsorbed onto the graphene surface in various configurations and the adsorption energies of the lowest energy configuration was taken. To obtain the density of states (DOS) single point calculations were performed on the optimized structures using a  $\Gamma$ -centered  $12 \times 12 \times 1$  grid of  $k$ -points.

### 3. Results and discussion

#### 3.1. Physicochemical characterization of anodically exfoliated graphene

The production of graphene nanosheets by anodic exfoliation of graphite was verified previous to the production of the nucleotide/graphene hybrids. The structural order of the graphene aerogels prepared in Section 2.2 was studied by Raman spectroscopy and compared with the graphite foil precursor (Fig. 3a). Both materials displayed three bands; the G band at  $\sim 1585 \text{ cm}^{-1}$  (related to vibrations of C–C tensions in structures with  $sp^2$  hybridizations), the D band at  $\sim 1355 \text{ cm}^{-1}$  associated with 6-membered ring breathing vibrations in aromatic structures (and active in Raman spectrum only when the ring is close to a structural defect) and 2D band at  $\sim 2721 \text{ cm}^{-1}$ , which is the overtone of the D band. A higher peak for G band means a higher-ordered structure with almost no defects while larger intensity of D band means the presence of defects. On the other hand, the less intense and wide is the 2D band, the lower is the number of defects. In addition, the symmetry

of the 2D band depends on the stacking of the sheets, where an asymmetrical band indicates an ordered/periodical stacking [99]. The graphene prepared here by electrochemical exfoliation presented an intense D peak together with a wide/low intensity 2D band (Fig. 3a), confirming the delamination of the graphite into graphene nanosheets.

The degree of oxidation of the obtained graphene nanosheets was evaluated by XPS (see the survey spectrum in Fig. 3b), which yielded an O/C atomic ratio of 0.12 [100]. From the high-resolution C 1s core-level spectrum (see inset to Fig. 3b), it was concluded that epoxy/alcohol (C–O species) and carbonyl (C=O) moieties were formed during the anodic exfoliation process. The generation of graphene nanosheets was confirmed by AFM, where nanosheets with a lateral size of 0.2–1.2  $\mu\text{m}$  and 2–3 nm in thickness (corresponding to few/several layer nanosheets) were noticed (Fig. 3c and d). It can therefore be concluded that graphite was effectively delaminated into graphene nanosheets with a moderate degree of oxidation. These parameters are crucial in achieving a stable interaction between graphene and the nucleotides; high accessible surface area and large aromatic (non-oxidized) domains to conduct a  $\pi$ - $\pi$  stacking [101]. Anchoring nucleotide-based electrocatalysts onto an electron-conductive material offers several advantages. Firstly, it enhances the kinetics of redox reactions, thereby facilitating efficient electron transfer. Secondly, it promotes the even dispersion of nucleotide catalysts, amplifying the active surface area available for catalytic reactions.

#### 3.2. Study of nucleotide solubility and graphene dispersibility in IPA/H<sub>2</sub>O media

The accessible surface area and electronically conjugated (aromatic) nature in the prepared graphene could facilitate the liquid phase

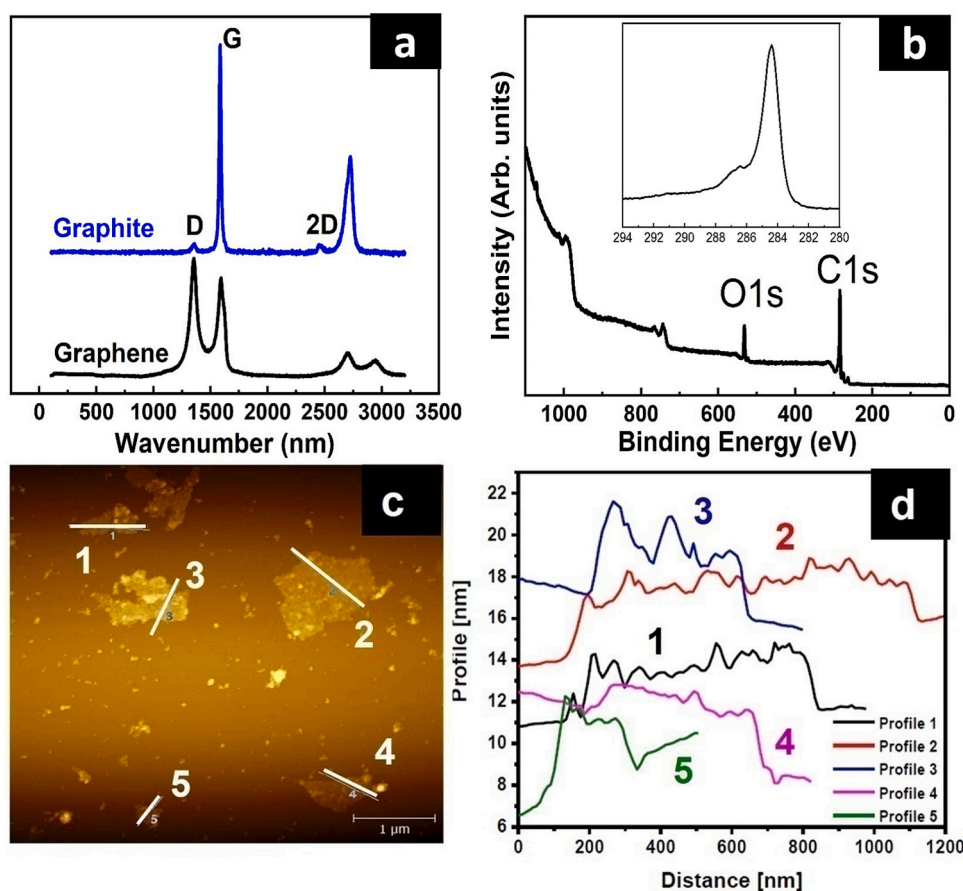


**Fig. 3.** a) Raman spectra of graphite foil and graphene after electrochemical exfoliation. b) XPS survey and high resolution C1s spectra (inset) for the obtained graphene. c) AFM images and d) AFM height profile of the anodically derived graphene nanosheets.



adsorption of the selected nucleotides on its surface. However, a suitable liquid media must be selected to ensure the colloidal stabilization of the graphene. Graphene nanosheets with moderate levels of oxidation, such as those investigated here, typically exhibit limited dispersibility in water alone. However, it is well-documented that alcohols can enhance the dispersion of graphene [102]. To assess the colloidal stability of graphene sheets, we conducted dispersion experiments in both IPA alcohol and H<sub>2</sub>O, generating two distinct dispersions in each solvent. The dispersions in H<sub>2</sub>O showed a severe aggregation of the graphene particles while those in IPA had negligible aggregation or sedimentation, even after storing for 24 h (Fig. S4a and S4b). It can be therefore concluded that IPA is a much better dispersant than H<sub>2</sub>O for the prepared graphene sheets. However, polar nucleotide salts are expected to be soluble in water, where a complete solubilization of the adsorbate is also necessary for efficient liquid adsorption. To find a compromise, a mixture of 35% IPA and 65% H<sub>2</sub>O (v/v %) was used based in previous studies on graphene dispersibility [66,103]. In fact, the anodically exfoliated graphene presented reasonable dispersibility in such IPA/H<sub>2</sub>O mixture, as shown in Fig. S4a and S4b. On the other hand, the solubility of the nucleotide salts was studied as described in Section 2.5. The IPA/H<sub>2</sub>O solution was supersaturated in each nucleotide salt, the concentration of the salt in the supernatant was measured by UV–vis absorption spectroscopy and the results are presented in Table 1. Unexpectedly, the supersaturation of the solvent with XMP, TMP, and CMP nucleotide salts caused a phase separation (Fig. S4c).

This phenomenon has been widely observed for biomolecules in response to changes in pH, temperature or ionic strength, and it is necessary for the completion of several biochemical processes [104,105]. To estimate the solubility of these nucleotides, their concentration in both phases, after separation, was measured and presented in Table 1. The predominant phase was based on H<sub>2</sub>O and contained a larger concentration of nucleotide (161–381 mg mL<sup>-1</sup>, as a function of the nucleotide XMP, TMP or CMP) compared with the second phase, which was enriched in IPA alcohol. Overall, the sum of the amount of salt present in both IPA and H<sub>2</sub>O phases was above 130 mg mL<sup>-1</sup> revealing a high solubility in the solvent media.

In contrast, GMP, IMP, and FMN did not present any phase separation upon supersaturation. These salts yielded much moderate solubility from 19 to 10 mg mL<sup>-1</sup> (0.05–0.02 mol L<sup>-1</sup>), where FMN was the least soluble nucleotide in the IPA/H<sub>2</sub>O mixture. Solubility is directly related to the ability of the nucleotides (solute) to interact with the solvent. In polar aqueous media, the solubility of the solute increases with the polarity of the molecular structure. As noticed in Fig. 2, the main difference in the molecular structure of the nucleotides lies in the nucleobase moiety. Nucleobases with just one aromatic ring (TMP and CMP) are those presenting higher solubility. This is reasonable, because additional 5-member (purines; e.g., IMP, GMP) or 6-membered (FMN) aromatic rings, which do not possess significant charge separation, tend to reduce the polarity of the molecule and therefore their solubility. In the case of XMP, the polarity of the nucleobase will be increased

significantly by the net negative charge present in the xanthine nucleobase due to deprotonation at the working pH.

This means that, for the mixed IPA/H<sub>2</sub>O solvent, the studied nucleotide salts can be divided into highly soluble (XMP, TMP and CMP) and poorly soluble (GMP, IMP and FMN). This is likely to govern their adsorption onto the graphene surface and potentially influence their loading, to form the final nucleotide/graphene hybrids. Considering the solubility values in Table 1, a nucleotide salt concentration of 5 mg mL<sup>-1</sup> (~ 0.01 mol L<sup>-1</sup>) was chosen for conducting the liquid-phase adsorption experiments. This concentration ensured the complete dissolution of low-solubility nucleotides while avoiding phase separation for those presenting higher solubilities.

### 3.3. Experimental quantification of nucleotide loading and validation through DFT simulations

The amount of nucleotide adsorbed/loaded onto the graphene nanosheets was calculated indirectly by UV–vis absorption spectroscopy from Eq. (1). Specifically, the IPA/H<sub>2</sub>O dispersion containing the graphene sheets and the adsorbed nucleotide was centrifugated after 24 h. The sediment comprising the nucleotide/graphene hybrid material was separated from the solution containing the non-adsorbed nucleotide salt (SP1), which was then analyzed. Additionally, after redispersing the first hybrid sediment in fresh IPA/H<sub>2</sub>O and re-centrifuging (SP2) the solution was also analyzed to consider whether nucleotide molecules could detach from the hybrid after the washing step (Fig. S2).

The quantification of nucleotide loading was somewhat challenging, as the nucleotides are amphiphilic and therefore tend to stabilize the graphene nanosheets in aqueous media when adsorbed on their surface (i.e. the graphene sheets in the hybrid material are colloiddally more stable than bare graphene). Specifically, the essentially hydrophobic, aromatic moiety in the nucleobase is expected to adsorb onto the basal plane of graphene through  $\pi$ - $\pi$  stacking interactions, while the hydrophilic, negatively charged phosphate as well as the pentose sugar interact with water molecules. In this regard, attaining clear transparent SP1 supernatant solutions by simple centrifugation was challenging because the improved colloidal stability of the graphene nanosheets prevented their complete sedimentation (see Fig. S5a). This led to inaccuracies in the UV–vis absorption spectroscopy measurements, as the nucleotides strongly absorb in a wavelength similar to that corresponding to the absorption peak for the anodic graphene (250–278 nm, Fig. S1). Therefore, any graphene nanosheets remaining in the supernatant solution will contribute to absorbance in the wavelength range used for nucleotide quantification, leading to an underestimation of the nucleotide concentration. Sedimentation of the dispersions was even more challenging after the washing step, where SP2 supernatants were clear and homogeneous but with an intense black color (Fig. S5a). This was ascribed to a lower ionic strength in the washed dispersion, where the concentration of the nucleotide salt in SP2 is reduced by replacing the solution with fresh solvent. This phenomenon was confirmed by adsorbing different concentrations of GMP salt (0.5 to 5 mg mL<sup>-1</sup>) on a 2 mg mL<sup>-1</sup> graphene dispersion for 24 h. After centrifugation, the black color in the supernatants increased as the initial concentration of the nucleotide salt decreased (Fig. S5b). It is hypothesized that Na<sup>+</sup> cations present in concentrated solutions of the nucleotide salt (which is the case in SP1, Fig. S5a) have an “ion-shielding” effect by neutralizing the negative charge on the nucleotide/graphene hybrids [106,107]. Thus, Na<sup>+</sup> cations accumulate around the phosphate groups and screen their negative charge. As a result, electrostatic repulsions between the nucleotides adsorbed on the graphene nanosheets, which are the main driver of their colloidal stability in aqueous medium, are significantly reduced. When washing the sample, the amount of Na<sup>+</sup> in the supernatant is significantly decreased, so charge screening of the phosphate groups is reduced, and the colloidal stability of the nucleotide/graphene hybrids increases. Bearing this in mind, an optically transparent salt was added to the dispersion in order to increase the ionic strength and

**Table 1**  
Solubility of nucleotide salts in IPA/H<sub>2</sub>O solvent measured by UV–vis absorption spectroscopy.

Nucleotide	Concentration (mg mL <sup>-1</sup> )		
	No phase separation	Phase separation	
		IPA/H <sub>2</sub> O	Fraction in H <sub>2</sub> O phase
XMP	–	381	73
IMP	14	–	–
GMP	19	–	–
TMP	–	275	139
CMP	–	161	87
FMN	10	–	–

promote the sedimentation of the hybrid material. The addition of 30 mg mL<sup>-1</sup> or 20 mg mL<sup>-1</sup> of NaCl to SP1 and SP2, respectively, enabled the correct quantification of free nucleotide by triggering the sedimentation of the small fraction of graphene nanosheets remaining in the supernatants (Fig. S5c). However, an increase in the ionic strength by the addition of NaCl caused a partial precipitation of low-soluble nucleotide salts; FMN, GMP and IMP as reported in Table 1. Hence, the addition of NaCl could decrease their saturation point which was already much lower than the other nucleotides. To estimate their precipitation threshold, NaCl salt concentrations ranging from 5 to 30 mg mL<sup>-1</sup> were added to IPA/H<sub>2</sub>O solutions containing only the nucleotide salts. XMP, TMP and CMP did not show any precipitation regardless of the amount of NaCl added. In contrast, the addition of concentrations of NaCl above 25 mg mL<sup>-1</sup> caused the sedimentation of IMP, GMP and FMN salts, particularly for the latter (Fig. S4d). Bearing this in mind, for low-soluble nucleotide salts, 20 and 10 mg mL<sup>-1</sup> of NaCl were added to SP1 and SP2 to get clean and transparent supernatants. The quantification of the nucleotide loading in the different hybrid materials obtained by UV-vis absorption spectroscopy is presented in Table 2.

The TGA profiles of the nucleotide/graphene hybrids, the stand-alone anodic graphene and pure nucleotide salts, recorded in an argon atmosphere up to 1000 °C, are shown in Fig. 4. The graphene material displayed a relatively minor mass loss below 200 °C due to the desorption of strongly adsorbed water molecules. Subsequently, a continuous weight loss was observed up to 1000 °C, vary likely arising from the decomposition of oxygen-containing functionalities into CO and CO<sub>2</sub> [100]. Such functional groups were indeed present in the graphene nanosheets, as demonstrated by XPS (Fig. 3b). At 1000 °C, the anodic graphene yielded a considerable residue (82 wt%), which was much larger than the residue typically left behind by standard graphene oxides [108]. This corroborated the idea that the present anodic graphene must possess a high fraction of electronically conjugated domains where aromatic molecules can readily adsorb. Regarding the nucleotides, a noticeable mass loss was observed between 200 and 400 °C for all the studied compounds. This reduction in weight can be attributed to the breakdown of the sugar-based component within the nucleotide, resulting in the formation of alcohol, ethylene, and acetaldehyde compounds [38,109,110]. The decomposition of pure nucleotide salts became more gradual above 400 °C. At this temperature, the nucleobase is likely decomposed into nitrogen compounds such as NH<sub>3</sub> or HCNO [38,74–77], while water is released due to phosphate condensation. At 1000 °C, a residue composed of a char, formed from the nucleobase and inorganic phosphate oxides, remained in the material [38,74]. The quantity of this residual material was consistent across all examined nucleotides, ranging from approximately 37% to 46% by weight. However, CMP exhibited the highest content among them. Similar to the behavior of the graphene support, the hybrid materials exhibited the release of water molecules trapped in the graphene structure at temperatures ranging from 150 to 200 °C. The decomposition curves of

HXMP (Fig. 4a), HIMP (Fig. 4b) and HCMP (Fig. 4e) closely resembled that of the anodic graphene alone, indicating minimal variations and implying low nucleotide loadings. In contrast, HGMP (Fig. 4c), HTMP (Fig. 4d) and HFMN (Fig. 4f) exhibited more distinct decomposition profiles associated to larger mass losses from 250 to 1000 °C, compared to graphene alone. Such a noticeable mass loss, starting at the decomposition temperature of the respective pure nucleotide, pointed to higher nucleotide loadings in the corresponding hybrids. The nucleotide loading was estimated from the TGA of hybrid materials. It was considered that the high-temperature treatment of the hybrid, under an inert atmosphere, will cause the decomposition of the organic nucleotide molecule but not the graphene. The registered mass loss will be therefore proportional to the amount of nucleotide loaded on the graphene support. However, as observed from the analysis of the TGA profiles for the stand-alone graphene and nucleotide salts, it must be considered that (1) the nucleotide left significant residue from phosphate/char formation and (2) graphene released some gases from oxygen functionalities. In this context, some assumptions described in Section 2.4 and Supporting Information were considered to formulate Eq. (2) and calculate the nucleotide loading values listed in Table 2.

We also successfully determined the nucleotide loading through XPS data analysis, utilizing the measurement of P and N elements as characteristic indicators of nucleotide presence. These corresponding values are presented in Table 2.

It is worth noting that the values of nucleotide loading obtained through TGA and XPS analyses exhibited greater overall consistency when compared to those acquired through UV-vis absorption spectroscopy. Nonetheless, a reliable estimation of nucleotide loading was obtained by calculating the average and standard deviation of the values obtained from the three techniques.

From this analysis, we conclude that GMP and FMN exhibit the most favorable adsorption on the graphene surface, as their corresponding hybrids exhibited the highest loadings (~25–26 wt%). In contrast, the HCMP hybrid showed the lowest nucleotide loading (9 wt%). HIMP, HTMP and HXMP yielded intermediate loadings (~15–19 wt%). Non-covalent  $\pi$ - $\pi$  stacking interactions are considered the main driver of nucleotide adsorption on the graphene surface. The  $\pi$  molecular orbitals of the aromatic nucleobase (Fig. 2) overlap with those of the electronically conjugated structure of graphene, determining their adsorption strength. Here, nucleotides having heterocycles with a larger number of aromatic rings (flavine > purine > pyrimidine) can be expected to exhibit higher adsorption strengths and thus higher loadings on graphene. Consistently, FMN and GMP demonstrated the largest loadings, whereas CMP showed the lowest. However, some inconsistencies in this trend were identified from the experimental data (Table 2): (1) IMP, XMP and GMP are composed of a two-ring purine, but the latter presented a higher loading than the other two nucleotides, and (2) TMP led to a higher loading than CMP, despite both having a one-ring pyrimidine motif in their structures. Therefore, the number of aromatic rings in the nucleobase cannot be the sole factor dictating the adsorption of the nucleotide on the graphene substrate. It has been reported that the substitution of carbon atoms in the aromatic ring by heteroatoms (*endo*-substitution) or the presence of functional groups attached to the ring (*exo*-substitution) can significantly modify the  $\pi$ -electron delocalization of the molecule [111]. All the nucleotides investigated here (Fig. 2) incorporate a highly polarizable endocyclic carbonyl (C=O) group in their nucleobases. This oxygen atom withdraws electronic density and prevents electron delocalization in the conjugated system by inducing a positive charge in the adjacent carbon atom. This phenomenon will decrease the aromaticity of the nucleobase and, consequently, the adsorption rate of the nucleotide. However, it has been reported that imide functionality in XMP, TMP and FMN nucleotides can delocalize electrons by external cross conjugation of the  $\pi$  orbitals in the aromatic ring with those from the C=O and N-H groups (Fig. S6a) [111,112]. Thus,  $\pi$ -electrons will be strongly delocalized in the ring and throughout the tautomeric system, including the *exo*-groups (i.e. the aromaticity of

**Table 2**

Experimental quantification of nucleotide loading for the different nucleotide/graphene hybrids and the corresponding theoretical adsorption energies of each nucleotide on a graphene layer.

Hybrid material	Experimental quantification (wt%)			Estimation for the experimental quantification (wt%) $\bar{X} \pm \sigma$ (UV-vis, TGA, XPS)	DFT calculations Adsorption energy (kcal mol <sup>-1</sup> )
	UV-vis	TGA	XPS		
HXMP	27	18	12	19 ± 6	-15
HIMP	24	15	8	16 ± 6	-30
HGMP	32	23	20	25 ± 5	-25
HTMP	12	20	12	15 ± 4	-16
HCMP	6	11	9	9 ± 2	-9
HFMN	26	22	31	26 ± 4	-48



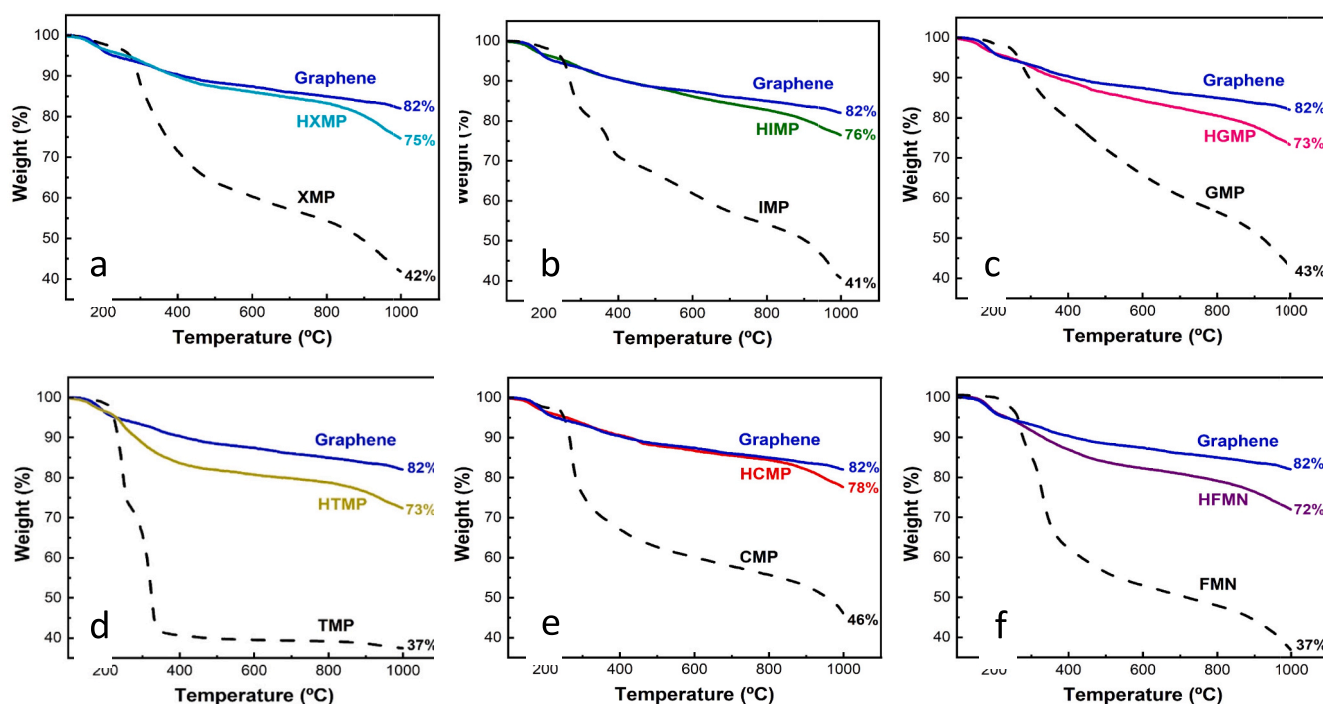


**Fig. 4.** TGA curves for the different nucleotide/graphene hybrids: a) HXMP, b) HIMP, c) HGMP, d) HTMP, e) HCMP, and f) HFMN. The TGA curves for anodic graphene alone (blue solid lines) and the corresponding pure nucleotides (black dashed lines) are shown for comparison.

the nucleobase increases). This effect will favor the adsorption of the nucleotides containing imide functionality onto the graphene surface, which would explain the higher adsorption of TMP and XMP compared with CMP and IMP, respectively. However, it does not explain the high loading observed for GMP, which does not have an imide group in its nucleobase (Fig. 2). The unexpectedly high adsorption rate of GMP compared with the other nucleotides could be ascribed to strong intermolecular bonding. The formation of intermolecular triple hydrogen bonding via the adjacent amine/carbonyl groups in the guanine nucleobase could change the aromatic character of the nucleotides. Strong intermolecular interactions can create dipoles by stabilization of tautomeric forms with charge separation in a nucleobase (Fig. S6b) [111]. In turn, the approximation of dipoles to the graphene surface can induce lattice distortion and electric dipole moment on the  $\pi$ -electron cloud, thus enabling a van der Waals interaction between polarized nucleobase ring in GMP and localized electrons in graphene. Such an intermolecular interaction could also be present in CMP, as it presents a similar structure to that of GMP in the 6-membered ring of the nucleobase. However, the nitrogen atom belonging to the pyrimidine ring in CMP is not protonated and, therefore, it cannot form a third hydrogen atom, which significantly reduces the charge polarization. This hypothesis is consistent with the results shown in Table 2, where the HCMP hybrid yielded the lowest loading. Also, pairing nucleotides with their complementary nucleobase provides stable hydrogen-bonded supramolecular entities that adsorb more strongly on the graphene surface than their individual components [65]. In this study, it is possible that the higher loading of GMP molecules is attributed to the stable association of identical nucleobases within the adsorbed GMP molecules. Thus, it can be inferred that the number of rings in the nucleobase governs nucleotide adsorption onto graphene, but electron delocalization via cross-conjugation in the imide functionality (as seen in XMP, TMP, and FMN) and the formation of intermolecular hydrogen bonds (in the case of GMP) also contribute to the determination of adsorption strength.

To complement the experimental work, the adsorption energies ( $E_{ad}$ ) of the different nucleotides on the graphene surface were determined

from DFT calculations following Eq. (8). The results are compared with nucleotide loading data obtained from the experimental quantification (Table 2), where a lower  $E_{ad}$  indicates a more favorable adsorption (exothermic process) [113,114]. We found that in the case of FMN, the lowest energy configuration was attained when the nucleotide adsorbed parallel to the graphene surface. Such a result can be explained by the establishment of strong  $\pi$ - $\pi$  stacking interactions in the parallel configuration. This is shown in Fig. S7, where  $E_{ad}$  values for two adsorption configurations of riboflavin (the nucleobase of FMN) are displayed. The geometry-optimized structures for each nucleotide system investigated here are shown in Fig. S8. From our DFT calculations, we find that in addition to the nucleobase adsorbing parallel to the graphene surface, the nucleotide side-chain (i.e., the phosphorylated sugar moiety) also tends to adsorb in alignment with the surface. Additionally, we found a slight tilt of the riboflavin heterocycle along the graphene sheet (also reported by Zdaniasienė [115]), indicating steric hindrance and preventing a perfect parallel arrangement of the molecule. The energy difference between these configurations is  $\sim 6$  kcal mol $^{-1}$  and in the presence of the phosphate group (FMN) the difference increased to  $\sim 12$  kcal mol $^{-1}$ . This led to FMN exhibiting the largest adsorption energy ( $-48$  kcal mol $^{-1}$ ) compared to the other purine-like nucleotides, which exhibit adsorption energies from  $-15$  to  $-30$  kcal mol $^{-1}$ . It seems that for the larger nucleotides there is more flexibility of the phosphorylated sugar sidechain with the DFT simulations showing a preference for the sidechain to adsorb parallel to the graphene surface, slightly increasing the overall strength of adsorption (Fig. S7). This is not found for the smaller pyrimidine nucleotides (TMP and CMP) and XMP which were seen to adsorb with their phosphorylated sugar side-chain non-aligned to the surface, as shown in Fig. S8. However, there may be somewhat of a trade-off as a larger molecule would lead to a lower total number of molecules being able to adsorb to the graphene surface. Excluding IMP, our simulations predict the experimentally observed order of nucleotide loading based adsorption strength. With respect to FMN and IMP, their large  $E_{ad}$  suggests that the amount of nucleotide adsorbed on graphene should be significantly higher. We attribute this difference to the configurational arrangement of the nucleotide on the graphene surface.

For FMN we found a difference between the two configurations of  $12 \text{ kcal mol}^{-1}$ , but for IMP the difference was found to be about  $19 \text{ kcal mol}^{-1}$ . These differences are relatively small, only slightly larger than the thermal energy at room temperature ( $\sim 6 \text{ kcal mol}^{-1}$ ). Therefore, we suggest that for FMN and IMP the molecules can readily switch between different configurations in vitro. In the case of XMP, our DFT results found the optimum geometry to be with the side-chain non-aligned to the surface, thus yielding a slightly lower  $E_{\text{ad}}$  of  $-15 \text{ kcal mol}^{-1}$ . Finally, the one-ring pyrimidines were found to have the lowest adsorption energies. TMP yielded a similar value ( $-16 \text{ kcal mol}^{-1}$ ) to that of XMP, and CMP exhibited the lowest energy from the whole series ( $-9 \text{ kcal mol}^{-1}$ ). However, the variation in  $E_{\text{ad}}$  was more subtle between molecules with the same number of rings.

It should be noted that the conditions under which the computational calculations were performed and the conditions in the laboratory were not identical. However, a reasonable coincidence in the adsorption trend between experimental results and computational calculations was observed, which lay the foundations for the theoretical screening of a huge number of synthetic derivatives of biologically inspired molecules.

### 3.4. Study of the nucleotide dispersion in the hybrid

As previously commented, the dispersion of a given electrocatalyst is

also a very important parameter in heterogeneous catalysis. Hence, exposure of the catalytic sites increases while the molecules are not agglomerated but arranged to form a monolayer, leading to a larger electrochemically active area. The nucleotide/graphene hybrids prepared in this work are envisaged as heterogeneous catalysts. Therefore, the dispersion of nucleotides (catalytically active component) on the graphene support was studied by SEM-EDX imaging of nitrogen and phosphorus (Fig. 5 and S9). The detection sensitivity of light elements by this technique is quite low. Consequently, the mapping of phosphorous atoms resulted in better images to estimate the dispersion of adsorbed nucleotides in contrast to nitrogen atoms (compare Fig. 5 and S9). The phosphorus signal (pink dots in Fig. 5) was homogeneously distributed throughout the surface of all the hybrid materials.

### 3.5. Study of the electrocatalytic activity of HFMN by RDE and validation through DFT simulations

The potential vs current density LSV curves for ORR and OER reactions of a selected hybrid material (HFMN) and bare graphene were displayed in Fig. 6a. The curves were acquired in separate experiments using different samples as working electrodes. The reduction of oxygen was studied in an aqueous alkaline electrolyte saturated in  $\text{O}_2$  while the oxidation was conducted under  $\text{N}_2$  atmosphere. The stability of the

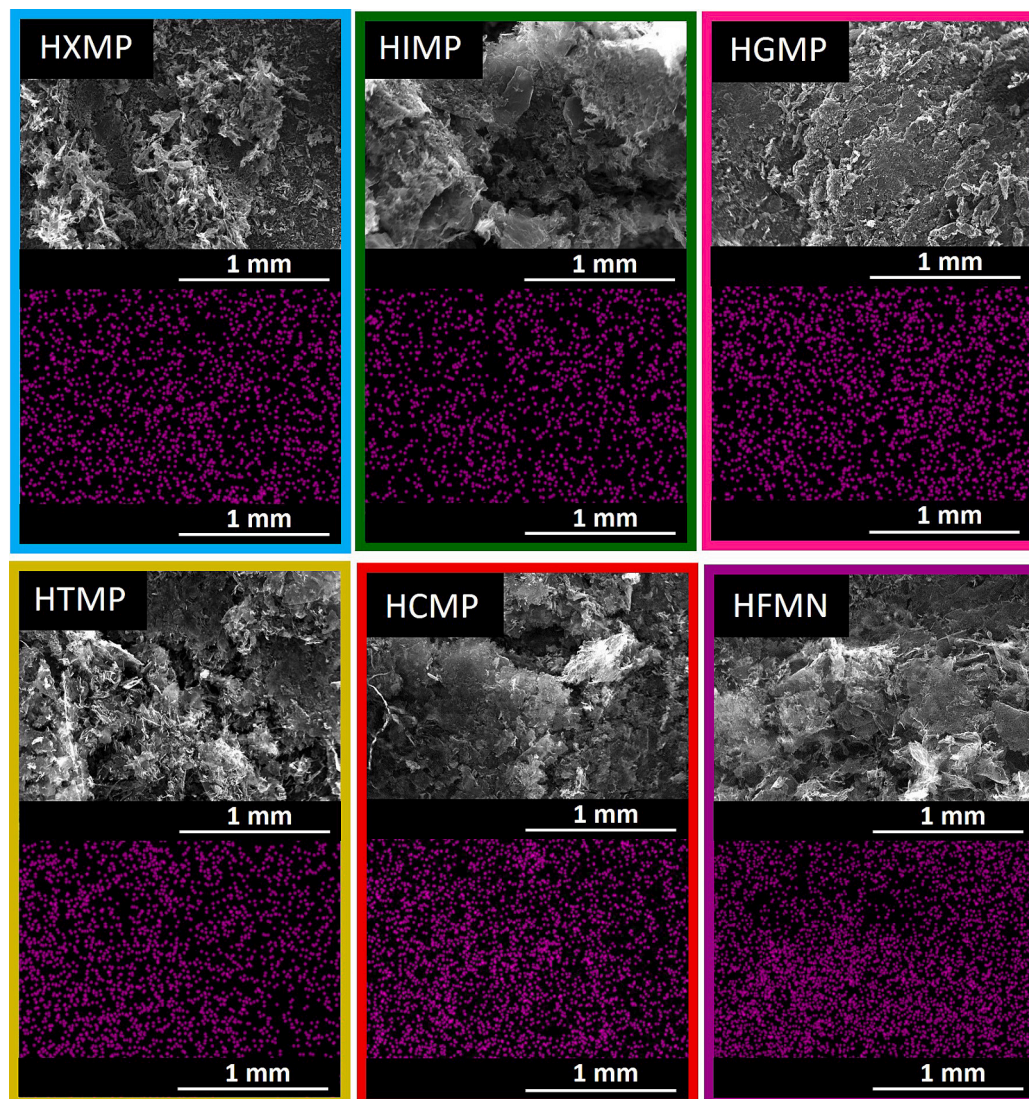
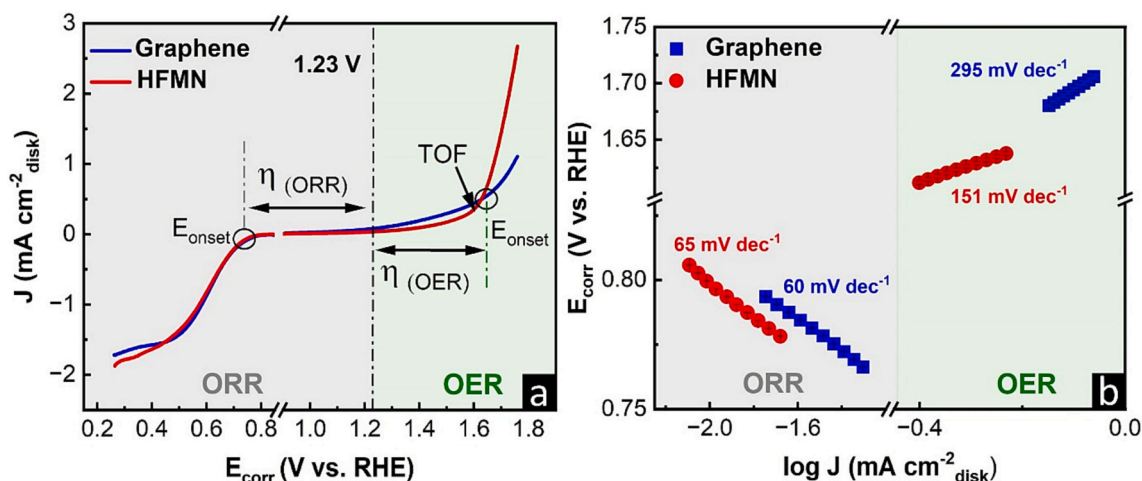


Fig. 5. SEM imaging and EDX mapping for phosphorous atoms (pink dots) in nucleotide/graphene hybrids.





**Fig. 6.** a) LSV curves in 0.1 M KOH electrolyte at 10 mV s<sup>-1</sup> and 1600 rpm for ORR (saturated in O<sub>2</sub>) and OER (saturated in N<sub>2</sub>) and b) Tafel plots for ORR and OER reactions.

materials studied in this work was verified by cyclic voltammetry (CV) and chronoamperometry (CA) measurements (see conditions and Figs. S10 and S11 in Supporting Information). No differences were observed in the CVs performed before and after the LSV measurements (Fig. S10), indicating that the materials studied were stable. Regarding CAs (Fig. S11), for ORR, the retention rates for graphene and HFMN were 26% and 22%. However, for OER, both materials exhibited low retention rates, 3% for graphene and 6% for HFMN, respectively. Therefore, it can be concluded that both materials demonstrated increased stability towards ORR. In general, these materials might exhibit less stability due to the harsh conditions in this work, i.e., the alkaline medium (pH = 13). However, it is expected that a neutral medium would promote the stability of these materials which will be the subject of study in future work. In relation to the LSV curve for ORR reaction (left gray part in Fig. 6a), HFMN hybrid material curve is almost identical to that in the graphene support. The anodic potential sweep led to a significant decrease in the current response at ~0.7 V (onset potential, E<sub>onset</sub>), signaling a reduction occurring at the cathode interface. The E<sub>onset</sub> was ~0.73 V for both graphene and HFMN materials (measured at -0.1 mA cm<sup>-2</sup>, Table 3), indicating similar catalytic efficiency for both materials. Furthermore, the Tafel slope, calculated for both materials (depicted in the left gray section of Fig. 6b) at the turning point where the current initiates a decline (indicating the kinetic-controlled region), showed striking similarity (Table 3). A Tafel slope close to 60 mV dec<sup>-1</sup> for ORR corresponds to a pseudo two-electron reaction as the rate-determining step [18,116–118]. This statement was demonstrated through Koutecky-Levich plots (Fig. S12) from which the number of electrons transferred was calculated (see measurement conditions in Supporting Information and the number of electrons transferred in Table S1). The parameter values obtained for both HFMN and graphene in the ORR were compared with graphene synthesized by

cathodic electrochemical exfoliation (Table S1), prepared by a similar method to that carried out in this work. [119] The results for E<sub>onset</sub>, j, n and E<sub>1/2</sub> were comparable except for the Tafel slope, where the graphene obtained by Jaimes-Paez et al. had a higher slope, 109 mV dec<sup>-1</sup>, respectively. Therefore, the graphene synthesized in this work catalyzed the ORR better. However, the number of electrons transferred was 2.5, indicating that, being at values of 2–2.5, all the materials compared follow the mechanism leading to H<sub>2</sub>O<sub>2</sub> formation [120]. For potentials below 0.4 V, the profile reaches a steady-state where the current density was not affected by the rate of mass transfer of O<sub>2</sub> from the electrolyte bulk to the electrode surface. The limiting current registered at this point serves as an indicator of the activity of the catalyst, with a higher value indicating a more rapid reaction rate. As observed from Fig. 6a, the HFMN hybrid did not show any increase in the limiting current density compared with bare graphene. In contrast, HFMN hybrid showed an improved activity towards OER reaction when compared with graphene support (right green part in Fig. 6a). The closer the E<sub>onset</sub> to the standard oxidation/reduction potential of oxygen (1.23 V vs. RHE), the higher is the efficiency of the catalyst [121,122]. In this regard, the E<sub>onset</sub> measured at +0.5 mA cm<sup>-2</sup> is slightly reduced from 1.630 V to 1.627 V by adsorption of FMN nucleotide on the graphene surface (Table 3). Although the E<sub>onset</sub> value is similar for graphene and hybrid material, the Tafel slope for the latter is lower (151 mV dec<sup>-1</sup> vs. 295 mV dec<sup>-1</sup>, Table 3 and right green section of Fig. 6b). This indicates a faster electron-transfer kinetics [123–125] for the hybrid, where a higher current density (2.68 vs. 1.11 mA cm<sup>-2</sup> at 1.75 V in Fig. 6a) is achieved for the same overpotential. The turnover frequency (TOF) for OER was calculated from the LSV curves at 1.60 V using Eq. (7) and displayed in Table 3. The calculation of the active sites was possible from the thorough quantification of the adsorbed FMN nucleotide conducted in Table 2. A higher TOF value in HFMN corroborates an improved efficiency for the hybrid material compared with graphene [126–128].

In summary, the adsorption of the FMN nucleotide onto the conductive graphene surface did not alter the electrocatalytic activity for ORR. Nevertheless, the improved performance observed for OER in the hybrid material is very promising, as this reaction represents a significant hurdle in the development of energy generation and storage technologies.

The results obtained in this work related to ORR and OER have been compared with conventional doping/functionalization based graphenes from literature (Table S1 and S2). In this work no thermal treatments were applied to the materials which were obtained by straightforward, sustainable and scalable processing (anodic exfoliation) of graphite to provide graphene and then simple adsorption of nucleotides on it.

**Table 3**

Different parameter values obtained in ORR and OER measurements for graphene and HFMN.

Sample	ORR		OER		
	E <sub>onset</sub> (V) (@ -0.1 mA cm <sup>-2</sup> )	Tafel slope (mV dec <sup>-1</sup> )	E <sub>onset</sub> (V) (@ +0.5 mA cm <sup>-2</sup> )	Tafel slope (mV dec <sup>-1</sup> )	TOF (s <sup>-1</sup> )
Graphene	0.739	60	1.630	295	1.81 × 10 <sup>-4</sup>
HFMN	0.730	65	1.627	151	1.5 × 10 <sup>-2</sup>

However, most of the studies in which graphene is doped with heteroatoms do not comply with these features (see the samples preparation in Table S1 and S2). Graphene oxide is generally used, which is obtained by Hummers method or its derivatives, which have drawbacks such as the production of toxic gases and the use of strong oxidizing agents [129–133]. In addition, heat treatments are used to functionalize the heteroatoms. Consequently, in terms of simplicity and environmental friendliness during their preparation (no need to use harsh reagents, no need to apply any heat treatment for reduction), the materials used in this work have a clear advantage compared with conventional doping/functionalization based graphenes.

DFT calculations were carried out to evaluate the experimental observations. The total DOS for HFMN is presented in Fig. 7, where we have also separated the total DOS into its individual contributions of the FMN nucleotide and the graphene surface. The Fermi level ( $E_F$ ) is set to zero. From our calculated DOS, we find the addition of FMN generates empty states in the conduction band just above the Fermi level. This may be beneficial for OER activity compared to just standalone graphene since these empty states may facilitate electron transfer. Thus, acceptor states could benefit the OER rather than the ORR, as the OER generates 4  $e^-$  that would need to be accepted in the electron transfer reaction. For the ORR there may be a lack of donor states for the reaction to proceed. Of course, this is not a simple process and would also depend on the adsorption of molecular oxygen, which certainly warrants further investigation in future studies.

#### 4. Conclusions

Nucleotide/graphene hybrid materials have been prepared using electrochemical exfoliated graphene by simple liquid adsorption. The amount of nucleotide adsorbed on the graphene surface from the liquid phase (i.e., the nucleotide loading) has been quantified by different techniques, where thermogravimetric analysis seems to be the best option when considering its simplicity and accuracy. We hypothesized that the adsorption of the nucleotide is favored by the aromatic character of the nucleobase, where three parameters dictate adsorption strength; 1) the number of rings on the nucleobase (e.g. FMN presents larger adsorption than CMP), 2) the presence of functional groups delocalizing the  $\pi$ -electrons outside the aromatic rings in the nucleobase (e.g. TMP and CMP yield one aromatic ring but imide group in the former lead to larger adsorption rate), and 3) the formation of nucleotide dimers through strong intermolecular hydrogen bonding (e.g. GMP exhibits a

larger adsorption yield than any other of the two-ringed nucleotides). Such strong intermolecular interactions could create dipoles in the nucleobase ring, enabling van der Waals interaction with instantaneous polarizations in the electron cloud of graphene. Also, the desorption of nucleotide dimers/clusters could be less favorable than for the single-ring nucleotides. Computational studies on the adsorption energy of the nucleotides on single layer graphene were consistent with the adsorption yields obtained by experimental quantification. In addition to loading, dispersion plays a crucial role in determining the (electro) catalyst's performance. SEM-EDX imaging confirmed that the nucleotides were homogeneously distributed/dispersed across the graphene surface. The quantification of different nucleotides loaded onto graphene nanosheets conducted in this work is expected to provide a starting point for the determination of the active sites in non-metallic electrocatalysts, enabling a suitable determination of their intrinsic catalytic activity. Overall, the methodology here presented paves the way for the development of metal-free electrocatalysts using natural and environmentally friendly chemistries while contributing to their reliable quantitative evaluation as potential electrocatalysts for new energy storage technologies.

Flavin monophosphate/graphene nucleotide was selected as the proof-of-concept material for studying the electrocatalytic activity of the prepared hybrid materials towards oxygen reduction and evolution reactions. The biomimetic material exhibited improved activity towards the evolution of oxygen, highlighting its considerable potential. This is particularly noteworthy as the oxygen evolution reaction is a major bottleneck in gas conversion technologies. Moreover, the computed density of states for the flavin monophosphate/graphene hybrid unveiled the presence of additional nucleotide-related empty states just above the Fermi level when compared with bare graphene, suggesting heightened electrocatalytic activity of this material towards the OER. The good alignment between experimental and computational studies paves the way for the discovery of innovative, sustainable, and efficient electrocatalyst inspired by natural molecules and processes.

#### CRediT authorship contribution statement

**A. Letona-Elizburu:** Writing – review & editing, Writing – original draft, Visualization, Validation, Methodology, Investigation, Formal analysis, Data curation, Conceptualization. **M. Enterría:** Writing – review & editing, Writing – original draft, Methodology, Investigation, Formal analysis, Conceptualization. **A. Aziz:** Writing – review & editing,

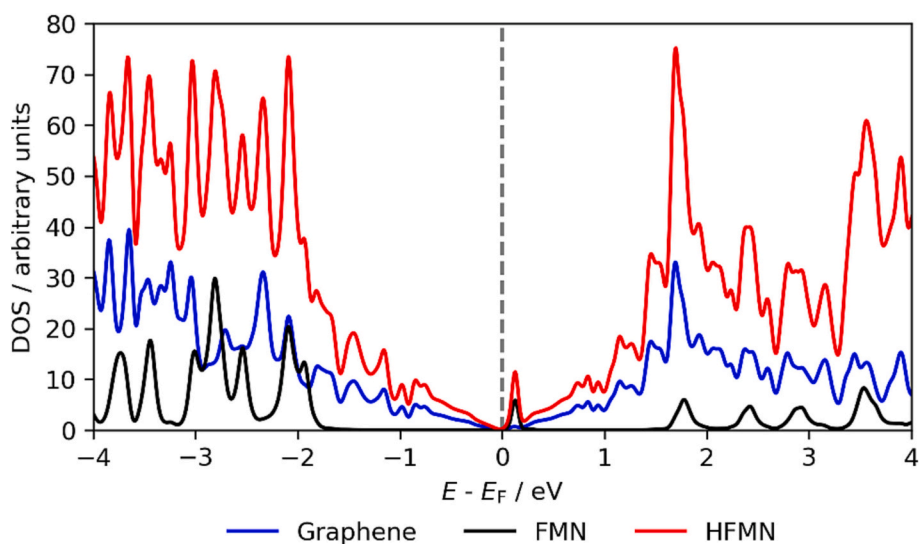


**Fig. 7.** Density of states as a function of energy, the Fermi level has been set to zero. The total DOS and the contributions from graphene and FMN are shown in red, blue and black, respectively.

Writing – original draft, Methodology, Investigation, Formal analysis, Data curation. **S. Villar-Rodil**: Writing – review & editing, Visualization, Validation, Investigation, Data curation. **J.I. Paredes**: Writing – review & editing, Formal analysis. **J. Carrasco**: Writing – review & editing, Software, Formal analysis. **N. Ortiz-Vitoriano**: Conceptualization, Formal Analysis, Funding acquisition, Methodology, Project administration, Resources, Supervision, Writing – original draft, Writing – review & editing.

## Declaration of competing interest

None.

## Data availability

Data will be made available on request.

## Acknowledgements

This work was funded by the R&D&I project PID2020–117626RA-I00, funded by MCIN/AEI/10.13039/501100011033. N. Ortiz-Vitoriano thanks Ramon y Cajal grant (RYC- 2020-030104-I) funded by MCIN/AEI/10.13039/501100011033 and by FSE invest in your future. The authors also thank SGI/IZO-SGIker UPV/EHU for providing supercomputing resources. Partial funding by the Spanish Ministerio de Ciencia e Innovación and Agencia Estatal de Investigación (MCIN/AEI/10.13039/501100011033) as well as the European Regional Development Fund (ERDF, A way of making Europe) through grant PID2021-125246OB-I00, and by Plan de Ciencia, Tecnología e Innovación (PCTI)2018-2022 del Principado de Asturias and the ERDF through grant IDI/2021/000037 is also gratefully acknowledged. The authors also gratefully acknowledge Dr. Zhang for AFM images, Dr. Cid for the graphene XPS and Ms. Medinilla for the SEM-EDX measurements.

## Appendix A. Supplementary data

Supplementary data to this article can be found online at <https://doi.org/10.1016/j.susmat.2024.e00835>.

## References

- [1] D.S. Falcão, A.M.F.R. Pinto, A review on PEM electrolyzer modelling: guidelines for beginners, *J. Clean. Prod.* 261 (2020) 121184, <https://doi.org/10.1016/j.jclepro.2020.121184>.
- [2] A. Morozan, B. Josselme, S. Palacin, Low-platinum and platinum-free catalysts for the oxygen reduction reaction at fuel cell cathodes, *Energy Environ. Sci.* 4 (2011) 1238–1254, <https://doi.org/10.1039/C0EE00601G>.
- [3] O. Lorenz, A. Kühne, M. Rudolph, W. Diyatmika, A. Prager, J.W. Gerlach, J. Griebel, S. Winkler, A. Lotnyk, A. Anders, B. Abel, Role of reaction intermediate diffusion on the performance of platinum electrodes in solid acid fuel cells, *Catalysts* 11 (2021) 1065, <https://doi.org/10.3390/CATAL11091065>.
- [4] X.-M. Lin, J.-F. Li, Applications of in situ Raman spectroscopy on rechargeable batteries and hydrogen energy systems, *ChemElectroChem* 10 (2023) e202201003, <https://doi.org/10.1002/celec.202201003>.
- [5] J. Wang, H. Kong, J. Zhang, Y. Hao, Z. Shao, F. Ciucci, Carbon-based electrocatalysts for sustainable energy applications, *Prog. Mater. Sci.* 116 (2021) 100717, <https://doi.org/10.1016/j.pmatsci.2020.100717>.
- [6] W. Smith, The role of fuel cells in energy storage, *J. Power Sources* 86 (2000) 74–83, [https://doi.org/10.1016/S0378-7753\(99\)00485-1](https://doi.org/10.1016/S0378-7753(99)00485-1).
- [7] M. Enterría, A. Letona-Elizburu, L. Medinilla, M. Echeverría, N. Ortiz-Vitoriano, Controlling the triple phase boundary on Na-O<sub>2</sub> battery cathodes with perfluorinated polymers, *Electrochim. Acta* 435 (2022) 141375, <https://doi.org/10.1016/j.electacta.2022.141375>.
- [8] X. Han, X. Li, J. White, C. Zhong, Y. Deng, W. Hu, T. Ma, Metal–air batteries: from static to flow system, *Adv. Energy Mater.* 8 (2018) 1801396, <https://doi.org/10.1002/AENM.201801396>.
- [9] F. Cheng, J. Chen, Metal–air batteries: from oxygen reduction electrochemistry to cathode catalysts, *Chem. Soc. Rev.* 41 (2012) 2172–2192, <https://doi.org/10.1039/C1CS15228A>.
- [10] Y. Li, J. Lu, Metal-air batteries: will they be the future electrochemical energy storage device of choice? *ACS Energy Lett.* 2 (2017) 1370–1377, <https://doi.org/10.1021/ACSENERGYLETT.7B00119>.
- [11] P.-X. Zhu, L.-C. Wang, F. Stewart, D. Ding, J. Matz, P. Dong, H. Ding, Direct conversion of natural gases in solid oxide cells: a mini-review, *Electrochim. Commun.* 128 (2021) 107068, <https://doi.org/10.1016/j.elecom.2021.107068>.
- [12] Y. Pei, H. Zhong, F. Jin, A brief review of electrocatalytic reduction of CO<sub>2</sub>—materials, reaction conditions, and devices, *Energy Sci. Eng.* 9 (2021) 1012–1032, <https://doi.org/10.1002/ESE3.935>.
- [13] B.H. Ko, B. Hasa, H. Shin, Y. Zhao, F. Jiao, Electrochemical reduction of gaseous nitrogen oxides on transition metals at ambient conditions, *J. Am. Chem. Soc.* 144 (2022) 1258–1266, <https://doi.org/10.1021/jacs.1c10535>.
- [14] T.B. Ferriday, P.H. Middleton, M.L. Kolhe, Review of the hydrogen evolution reaction—abasic approach, *Energies* 14 (2021) 8535, <https://doi.org/10.3390/EN14248535>.
- [15] V. Rai, K.P. Lee, D. Safanama, S. Adams, D.J. Blackwood, Oxygen reduction and evolution reaction (ORR and OER) bifunctional electrocatalyst operating in a wide pH range for cathodic application in Li-air batteries, *ACS Appl. Energy Mater.* 3 (2020) 9417–9427, <https://doi.org/10.1021/ACSAEM.0C01775>.
- [16] K. Wiranarongkorn, K. Eamsiri, Y.-S. Chen, A. Arpornwichanop, A comprehensive review of electrochemical reduction of CO<sub>2</sub> to methanol: technical and design aspects, *J. CO<sub>2</sub> Util.* 71 (2023) 102477, <https://doi.org/10.1016/j.jcou.2023.102477>.
- [17] Y. Cong, B. Yi, Y. Song, Hydrogen oxidation reaction in alkaline media: from mechanism to recent electrocatalysts, *Nano Energy* 44 (2018) 288–303, <https://doi.org/10.1016/j.nanoen.2017.12.008>.
- [18] R. Ma, G. Lin, Y. Zhou, Q. Liu, T. Zhang, G. Shan, M. Yang, J. Wang, A review of oxygen reduction mechanisms for metal-free carbon-based electrocatalysts, *npj Comput. Mater.* 5 (2019) 1–15, <https://doi.org/10.1038/s41524-019-0210-3>.
- [19] N. Dubouis, A. Grimaud, The hydrogen evolution reaction: from material to interfacial descriptors, *Chem. Sci.* 10 (2019) 9165–9181, <https://doi.org/10.1039/c9sc03831k>.
- [20] H.-S. Kim, J.-Y. Lee, J.-K. Yoo, W.-H. Ryu, Capillary-driven formation of iron nanoparticles embedded in nanotubes for catalyzed lithium-carbon dioxide reaction, *ACS Mater. Lett.* 3 (2021) 815–825, <https://doi.org/10.1021/ACSMATERIALSLETT.1C00078>.
- [21] Q. Li, X. Rao, J. Sheng, J. Xu, J. Yi, Y. Liu, J. Zhang, Energy storage through CO<sub>2</sub> electroreduction: a brief review of advanced Sn-based electrocatalysts and electrodes, *J. CO<sub>2</sub> Util.* 27 (2018) 48–59, <https://doi.org/10.1016/j.jcou.2018.07.004>.
- [22] D.L. Dubois, Development of molecular electrocatalysts for energy storage, *Inorg. Chem.* 53 (2014) 3935–3960, <https://doi.org/10.1021/IC4026969>.
- [23] X. Duan, J. Xu, Z. Wei, J. Ma, S. Guo, H. Liu, S. Dou, Atomically thin transition-metal Dichalcogenides for Electrocatalysis and energy storage, *Small Meth.* 1 (2017) 1700156, <https://doi.org/10.1002/SMTD.201700156>.
- [24] Y. Qiao, J. Yi, S. Wu, Y. Liu, S. Yang, P. He, H. Zhou, Li-CO<sub>2</sub> electrochemistry: a new strategy for CO<sub>2</sub> fixation and energy storage, *Joule* 1 (2017) 359–370, <https://doi.org/10.1016/j.joule.2017.07.001>.
- [25] J. Deng, S. Fang, Y. Fang, Q. Hao, L. Wang, Y.H. Hu, Multiple roles of graphene in electrocatalysts for metal-air batteries, *Catal. Today* 409 (2023) 2–22, <https://doi.org/10.1016/j.cattod.2022.01.003>.
- [26] S. Park, Y. Shao, J. Liu, Y. Wang, Oxygen electrocatalysts for water electrolyzers and reversible fuel cells: status and perspective, *Energy, Environ. Sci.* 5 (2012) 9331–9344, <https://doi.org/10.1039/C2EE22554A>.
- [27] S. Zhao, L. Yan, H. Luo, W. Mustain, H. Xu, Recent progress and perspectives of bifunctional oxygen reduction/evolution catalyst development for regenerative anion exchange membrane fuel cells, *Nano Energy* 47 (2018) 172–198, <https://doi.org/10.1016/j.nanoen.2018.02.015>.
- [28] X. Wei, S. Cao, H. Xu, C. Jiang, Z. Wang, Y. Ouyang, X. Lu, F. Dai, D. Sun, Novel two-dimensional metal organic frameworks: high-performance bifunctional electrocatalysts for OER/ORR, *ACS Mater. Lett.* 4 (2022) 1991–1998, <https://doi.org/10.1021/ACSMATERIALSLETT.2C00694>.
- [29] J. Wei, D. Ng, M. Tang, T.F. Jaramillo, A Carbon-Free, Precious-Metal-Free, High-Performance O<sub>2</sub> Electrode for Regenerative Fuel Cells and Metal-Air Batteries, 2014, <https://doi.org/10.1039/c3ee44059a>.
- [30] J.W.D. Ng, Y. Gorlin, T. Hatsukade, T.F. Jaramillo, A precious-metal-free regenerative fuel cell for storing renewable electricity, *Adv. Energy Mater.* 3 (2013) 1545–1550, <https://doi.org/10.1002/AENM.201300492>.
- [31] X. Mu, S. Liu, L. Chen, S. Mu, Alkaline hydrogen oxidation reaction catalysts: insight into catalytic mechanisms, classification, activity regulation and challenges, *Small Struct.* 4 (2023) 2200281, <https://doi.org/10.1002/SSTR.202200281>.
- [32] Z.-L. Wang, D. Xu, J.-J. Xu, X.-B. Zhang, Oxygen electrocatalysts in metal–air batteries: from aqueous to nonaqueous electrolytes, *Chem. Soc. Rev.* 43 (2014) 7746–7786, <https://doi.org/10.1039/C3CS60248F>.
- [33] Y.-J. Wang, B. Fang, D. Zhang, A. Li, D.P. Wilkinson, A. Ignaszak, L. Zhang, J. Zhang, A review of carbon-composited materials as air-electrode bifunctional electrocatalysts for metal–air batteries, *Electrochim. Energy Rev.* 1 (2018) 1–34, <https://doi.org/10.1007/S41918-018-0002-3>.
- [34] L. Sharma, R. Gond, B. Senthilkumar, A. Roy, P. Barpanda, Fluorophosphates as efficient bifunctional electrocatalysts for metal–air batteries, *ACS Catal.* 10 (2020) 43–50, <https://doi.org/10.1021/ACSCATAL.9B03686>.
- [35] L. Xiong, Y. Qiu, X. Peng, Z. Liu, P.K. Chu, Electronic structural engineering of transition metal-based electrocatalysts for the hydrogen evolution reaction, *Nano Energy* 104 (2022) 107882, <https://doi.org/10.1016/j.nanoen.2022.107882>.
- [36] F. Song, L. Bai, A. Moysiadou, S. Lee, C. Hu, L. Liardet, X. Hu, Transition metal oxides as electrocatalysts for the oxygen evolution reaction in alkaline solutions:



- an application-inspired renaissance, *J. Am. Chem. Soc.* 140 (2018) 7748–7759, <https://doi.org/10.1021/JACS.8B04546>.
- [37] K. Zhang, R. Zou, Advanced transition metal-based OER Electrocatalysts: current status, Opportunities, and Challenges, *Small* 17 (2021) 2100129, <https://doi.org/10.1002/SMLL.202100129>.
- [38] M. Enterría, J. Luis Gómez-Urbano, J.M. Munuera, S. Villar-Rodil, D. Carriazo, J. I. Paredes, N. Ortiz-Vitoriano, Boosting the performance of graphene cathodes in Na–O<sub>2</sub> batteries by exploiting the multifunctional character of small biomolecules, *Small* 17 (2021) 2005034, <https://doi.org/10.1002/SMLL.202005034>.
- [39] B. Winther-Jensen, D.R. MacFarlane, New generation, metal-free electrocatalysts for fuel cells, solar cells and water splitting, *energy, Environ. Sci.* 4 (2011) 2790–2798, <https://doi.org/10.1039/C0EE00652A>.
- [40] V.B. Jaryal, A. Villa, N. Gupta, Metal-free carbon-based nanomaterials: insights from synthesis to applications in sustainable catalysis, *ACS Sustain. Chem. Eng.* 11 (2023) 14841–14865, <https://doi.org/10.1021/ACSSUSCHEMENG.3C01452>.
- [41] K.R.D. Kasibhatta, I. Madakannu, I. Prasanthi, Hetero atom doped graphene Nanoarchitectonics as Electrocatalysts towards the oxygen reduction and evolution reactions in acidic medium, *J. Inorg. Organomet. Polym. Mater.* 31 (2021) 1859–1876, <https://doi.org/10.1007/S10904-020-01834-W>.
- [42] J.S. Park, D.W. Chang, Iron Phthalocyanine/graphene composites as promising Electrocatalysts for the oxygen reduction reaction, *Energies* 13 (2020) 4073, <https://doi.org/10.3390/EN13164073>.
- [43] C. Hwang, J.T. Yoo, G.Y. Jung, S.H. Joo, J. Kim, A. Cha, J.-G. Han, N.-S. Choi, S. J. Kang, S.-Y. Lee, S.K. Kwak, H.-K. Song, Biomimetic superoxide disproportionation catalyst for anti-aging Lithium-oxygen batteries, *ACS Nano* 13 (2019) 9190–9197, <https://doi.org/10.1021/ACS.NANO.9B03525>.
- [44] L. Wang, Y. Wang, Y. Qiao, S. Wu, X. Lu, J.-J. Zhu, J.-R. Zhang, H. Zhou, Superior efficient rechargeable lithium–air batteries using a bifunctional biological enzyme catalyst, *energy, Environ. Sci.* 13 (2020) 144–151, <https://doi.org/10.1039/C9EE02652E>.
- [45] V.S. Sapner, P.P. Chavan, A.V. Munde, U.S. Sayyad, B.R. Sathe, Heteroatom (N, O, and S)-based biomolecule-functionalized graphene oxide: bifunctional Electrocatalyst for enhancing hydrazine oxidation and oxygen reduction reactions, *Energy Fuel* 35 (2021) 6823–6834, <https://doi.org/10.1021/ACS.ENERGYFUELS.0C04298>.
- [46] D. Nolfi-Donagan, A. Braganza, S. Shiva, Mitochondrial electron transport chain: oxidative phosphorylation, oxidant production, and methods of measurement, *Redox Biol.* 37 (2020) 101674, <https://doi.org/10.1016/J.REDOX.2020.101674>.
- [47] R.N. Kujundžić, N. Zarković, K.G. Trošelj, Pyridine nucleotides in regulation of cell death and survival by redox and non-redox reactions, *Crit. Rev. Eukaryot. Gene Expr.* 24 (2014) 287–309, <https://doi.org/10.1615/critrevukaryotgeneexpr.2014011828>.
- [48] M.L. Circu, R.E. Maloney, T.Y. Aw, Disruption of pyridine nucleotide redox status during oxidative challenge at normal and low-glucose states: implications for cellular adenosine triphosphate, mitochondrial respiratory activity, and reducing capacity in colon epithelial cells, *Antioxid. Redox Signal.* 14 (2011) 2151–2162, <https://doi.org/10.1089/ARS.2010.3489>.
- [49] C. Yang, Z. Liu, Metal Oxide-Based Nanostructured Electrocatalysts for Fuel Cells, Electrolyzers, and Metal-Air Batteries, Elsevier, 2021, <https://doi.org/10.1016/B978-0-12-818496-7.00002-3>.
- [50] C. Sathiskumar, S. Ramakrishnan, M. Vinothkannan, A.R. Kim, S. Karthikeyan, D. J. Yoo, Nitrogen-doped porous carbon derived from biomass used as trifunctional Electrocatalyst toward oxygen reduction, oxygen evolution and hydrogen evolution reactions, *Nanomaterials* 10 (2019), <https://doi.org/10.3390/NANO10010076>.
- [51] Z. Guo, D. Zhou, X. Dong, Z. Qiu, Y. Wang, Y. Xia, Ordered hierarchical mesoporous/macroporous carbon: a high-performance catalyst for rechargeable Li–O<sub>2</sub> batteries, *Adv. Mater.* 25 (2013) 5668–5672, <https://doi.org/10.1002/ADMA.201302459>.
- [52] D.U. Lee, P. Xu, Z.P. Cano, A.G. Kashkooli, M.G. Park, Z. Chen, Recent progress and perspectives on bi-functional oxygen electrocatalysts for advanced rechargeable metal-air batteries, *J. Mater. Chem. A Mater.* 4 (2016) 7107–7134, <https://doi.org/10.1039/C6TA00173D>.
- [53] C. Hu, R. Paul, Q. Dai, L. Dai, Carbon-based metal-free electrocatalysts: from oxygen reduction to multifunctional electrocatalysis, *Chem. Soc. Rev.* 50 (2021) 11785–11843, <https://doi.org/10.1039/D1CS00219H>.
- [54] D.K. Singh, R.N. Jenjeti, S. Sampath, M. Eswaramoorthy, Two in one: N-doped tubular carbon nanostructure as an efficient metal-free dual electrocatalyst for hydrogen evolution and oxygen reduction reactions, *J. Mater. Chem. A Mater.* 5 (2017) 6025–6031, <https://doi.org/10.1039/C6TA11057F>.
- [55] R. Paul, Q. Dai, C. Hu, L. Dai, Ten years of carbon-based metal-free electrocatalysts, *Carbon Energy* 1 (2019) 19–31, <https://doi.org/10.1002/CEY2.5>.
- [56] R. Paul, L. Zhu, H. Chen, J. Qu, L. Dai, Recent advances in carbon-based metal-free Electrocatalysts, *Adv. Mater.* 31 (2019) 1806403, <https://doi.org/10.1002/ADMA.201806403>.
- [57] F. Peng, Y. Lim, B. Kim, H.S. Kim, Z. Li, Z. Zhou, J. Li, W.H. Ryu, Blooming growth of durable carbon nanotubes bundles from graphite interlayer seeds for free-standing lithium-oxygen battery electrodes, *Sustain. Mater. Technol.* 35 (2023) e00531, <https://doi.org/10.1016/J.SUSMAT.2022.E00531>.
- [58] H.-S. Kim, B. Kim, H.-D. Lim, W.-H. Ryu, Self-oxygenated blood protein-embedded nanotube catalysts for longer Cyclable Lithium oxygen-breathing batteries, *ACS Sustain. Chem. Eng.* 10 (2022) 4198–4205, <https://doi.org/10.1021/acssuschemeng.1c08609>.
- [59] R. Li, Z. Wei, X. Gou, Nitrogen and phosphorus dual-doped graphene/carbon Nanosheets as bifunctional Electrocatalysts for oxygen reduction and evolution, *ACS Catal.* 5 (2015) 4133–4142, <https://doi.org/10.1021/ACSCATAL.5B00601>.
- [60] L. Feng, L. Wu, X. Qu, New horizons for diagnostics and therapeutic applications of graphene and graphene oxide, *Adv. Mater.* 25 (2013) 168–186, <https://doi.org/10.1002/ADMA.201203229>.
- [61] S. Gowtham, R.H. Scheicher, R. Ahuja, R. Pandey, S.P. Karna, Physisorption of nucleobases on graphene: density-functional calculations, *Phys. Rev. B* 76 (2007), <https://doi.org/10.1103/PHYSREVB.76.033401>.
- [62] S. Akca, A. Foroughi, D. Frochtzjwaj, H.W.C. Postma, Competing interactions in DNA assembly on graphene, *PLoS One* 6 (2011) 18442, <https://doi.org/10.1371/JOURNAL.PONE.0018442>.
- [63] G. Tuci, C. Zafferoni, A. Rossin, A. Milella, L. Luconi, M. Innocenti, L. Truong Phuoc, C. Duong-Viet, C. Pham-Huu, G. Giambastiani, Chemically functionalized carbon nanotubes with pyridine groups as easily tunable N-decorated nanomaterials for the oxygen reduction reaction in alkaline medium, *Chem. Mater.* 26 (2014) 3460–3470, <https://doi.org/10.1021/CM500805C>.
- [64] Y. Xu, C. Chen, M. Zhou, G. Fu, Y. Zhao, Y. Chen, Improved oxygen reduction activity of carbon nanotubes and graphene through adenine functionalization, *RSC Adv.* 7 (2017) 26722–26728, <https://doi.org/10.1039/C7RA02865B>.
- [65] B. Caridad, J.I. Paredes, O. Pérez-Vidal, S. Villar-Rodil, A. Pagán, J.L. Cenis, A. Martínez-Alonso, J.M.D. Tascón, A biosupramolecular approach to graphene: complementary nucleotide-nucleobase combinations as enhanced stabilizers towards aqueous-phase exfoliation and functional graphene-nucleotide hydrogels, *Carbon* 129 (2018) 321–334, <https://doi.org/10.1016/J.CARBON.2017.12.007>.
- [66] J.M. Munuera, J.I. Paredes, S. Villar-Rodil, A. Castro-Muñiz, A. Martínez-Alonso, J.M.D. Tascón, High quality, low-oxidized graphene via anodic exfoliation with table salt as an efficient oxidation-preventing co-electrolyte for water/oil remediation and capacitive energy storage applications, *Appl. Mater. Today* 11 (2018) 246–254, <https://doi.org/10.1016/J.APMT.2018.03.002>.
- [67] M. Ayán-Varela, J.I. Paredes, L. Guardia, S. Villar-Rodil, J.M. Munuera, M. Díaz-González, C. Fernández-Sánchez, A. Martínez-Alonso, J.M.D. Tascón, Achieving extremely concentrated aqueous dispersions of graphene flakes and catalytically efficient graphene-metal nanoparticle hybrids with flavin mononucleotide as a high-performance stabilizer, *ACS Appl. Mater. Interfaces* 7 (2015) 10293–10307, <https://doi.org/10.1021/ACSAMI.5B00910>.
- [68] W.L.F. Armarego, C.L.L. Chai, Purification of Laboratory Chemicals, 2003, p. 609.
- [69] K.N. Rogstad, Y.H. Jang, L.C. Sowers, W.A. Goddard, First principles calculations of the pKa values and Tautomers of Isoguanine and xanthine, *Chem. Res. Toxicol.* 16 (2003) 1455–1462, <https://doi.org/10.1021/TK034068E>.
- [70] M. Alves Fortunato, D. Aubert, C. Capdeillayre, C. Daniel, A. Hadjar, A. Princivalle, C. Guizard, P. Vernoux, Dispersion measurement of platinum supported on Yttria-stabilised zirconia by pulse H<sub>2</sub> chemisorption, *Appl. Catal. A Gen.* 403 (2011) 18–24, <https://doi.org/10.1016/j.apcata.2011.06.005>.
- [71] L.I. Van Der Wal, J. Oenema, L.C.J. Smulders, N.J. Samplonius, K.R. Nandpersad, J. Zečević, K.P. De Jong, Control and impact of metal loading heterogeneities at the nanoscale on the performance of Pt/zeolite y catalysts for alkane Hydroconversion, *ACS Catal.* 11 (2021) 3842–3855, <https://doi.org/10.1021/ACSCATAL.1C00211>.
- [72] J.A. Martins, A.C. Faria, M.A. Soria, C.V. Miguel, A.E. Rodrigues, L.M. Madeira, CO<sub>2</sub> methanation over hydrothermalite-derived nickel/ruthenium and supported ruthenium catalysts, *Catalysts* 9 (2019) 1008, <https://doi.org/10.3390/CATAL9121008>.
- [73] W. Wang, Z. Wang, J. Wang, C.-J. Zhong, C.-J. Liu, Highly active and stable Pt–Pd alloy catalysts synthesized by room-temperature Electron reduction for oxygen reduction reaction, *Adv. Sci.* 4 (2017) 1600486, <https://doi.org/10.1002/ADVS.201600486>.
- [74] F. Suárez-García, A. Martínez-Alonso, J.M.D. Tascón, Activated carbon fibers from Nomex by chemical activation with phosphoric acid, *Carbon* 42 (2004) 1419–1426, <https://doi.org/10.1016/J.CARBON.2003.11.011>.
- [75] M.A. Posthumus, N.M.M. Nibbering, A.J.H. Boerboom, H.-R. Schulten, Pyrolysis mass spectrometric studies on nucleic acids, *Biomed. Mass Spectrom.* 1 (1974) 352–357, <https://doi.org/10.1002/BMS.1200010512>.
- [76] J. Alongi, A. Di Blasio, J. Milnes, G. Malucelli, S. Bourbigot, B. Kandola, G. Camino, Thermal degradation of DNA, an all-in-one natural intumescent flame retardant, *Polym. Degrad. Stab.* 113 (2015) 110–118, <https://doi.org/10.1016/J.POLYMEDEGRADSTAB.2014.11.001>.
- [77] X.-J. Wang, J.Z. You, Study on the molecular structure and thermal stability of purine nucleoside analogs, *J. Anal. Appl. Pyrolysis* 111 (2015) 1–14, <https://doi.org/10.1016/J.JAAP.2014.12.024>.
- [78] R. Sanchis-Gual, A. Seijas-DaSilva, M. Coronado-Puchau, T.F. Otero, G. Abellán, E. Coronado, Improving the onset potential and Tafel slope determination of earth-abundant water oxidation electrocatalysts, *Electrochim. Acta* 388 (2021) 138613, <https://doi.org/10.1016/j.electacta.2021.138613>.
- [79] S. Anantharaj, P.E. Karthik, S. Noda, The significance of properly reporting turnover frequency in Electrocatalysis research, *Angew. Chem. Int. Ed.* 60 (2021) 23051–23067, <https://doi.org/10.1002/ANIE.202110352>.
- [80] M. Enterría, R. Mysyk, L. Medinilla, S. Villar-Rodil, J.I. Paredes, I. Rincón, F. J. Fernández-Carretero, K. Gómez, J.M. López del Amo, N. Ortiz-Vitoriano, Increasing the efficiency and cycle life of Na–O<sub>2</sub> batteries based on graphene cathodes with heteroatom doping, *Electrochim. Acta* 445 (2023) 142056, <https://doi.org/10.1016/J.ELECTACTA.2023.142056>.
- [81] E. Gileadi, E. Kirova-Eisner, Some observations concerning the Tafel equation and its relevance to charge transfer in corrosion, *Corros. Sci.* 47 (2005) 3068–3085, <https://doi.org/10.1016/J.CORSCI.2005.05.044>.

- [82] Q. Yin, Z. Xu, T. Lian, D.G. Musaev, C.L. Hill, Y.V. Geletii, Tafel slope analyses for homogeneous catalytic reactions, *Catalysts* 11 (2021) 87, <https://doi.org/10.3390/catal11010087>.
- [83] O.A. Petrii, R.R. Nazmutdinov, M.D. Bronshtein, G.A. Tsirlina, Life of the Tafel equation: current understanding and prospects for the second century, *Electrochim. Acta* 52 (2007) 3493–3504, <https://doi.org/10.1016/j.electacta.2006.10.014>.
- [84] Y. Irmawati, B. Prakoso, F. Balqis, N. Indriyati, R. Yudianti, F. Iskandar, A. Sumboja, Advances and perspective of Noble-metal-free nitrogen-doped carbon for pH-universal oxygen reduction reaction catalysts, *Energy Fuel* 37 (2023) 4858–4877, <https://doi.org/10.1021/ACS.ENERGYFUELS.2C04272>.
- [85] G. Zhong, S. Xu, L. Liu, C.Z. Zheng, J. Dou, F. Wang, X. Fu, W. Liao, H. Wang, Effect of experimental operations on the limiting current density of oxygen reduction reaction evaluated by rotating-disk electrode, *ChemElectroChem* 7 (2020) 1107–1114, <https://doi.org/10.1002/CELC.201902085>.
- [86] G. Kresse, J. Hafner, Ab initio molecular-dynamics simulation of the liquid-metal-amorphous-semiconductor transition in germanium, *Phys. Rev. B* 49 (1994) 14251–14269, <https://doi.org/10.1103/PHYSREVB.49.14251>.
- [87] G. Kresse, J. Hafner, Ab initio molecular dynamics for liquid metals, *Phys. Rev. B* 47 (1993) 558–561, <https://doi.org/10.1103/PHYSREVB.47.558>.
- [88] G. Kresse, J. Furthmüller, Efficient iterative schemes for ab initio total-energy calculations using a plane-wave basis set, *Phys. Rev. B* 54 (1996) 11169–11186, <https://doi.org/10.1103/PHYSREVB.54.11169>.
- [89] G. Kresse, J. Furthmüller, Efficiency of ab-initio total energy calculations for metals and semiconductors using a plane-wave basis set, *Comput. Mater. Sci.* 6 (1996) 15–50, [https://doi.org/10.1016/0927-0256\(96\)00008-0](https://doi.org/10.1016/0927-0256(96)00008-0).
- [90] J.P. Perdew, K. Burke, M. Ernzerhof, Generalized gradient approximation made simple, *Phys. Rev. Lett.* 77 (1996) 3865–3868, <https://doi.org/10.1103/PHYSREVLETT.77.3865>.
- [91] P.E. Blöchl, Projector augmented-wave method, *Phys. Rev. B* 50 (1994) 17953, <https://doi.org/10.1103/PhysRevB.50.17953>.
- [92] G. Kresse, D. Joubert, From ultrasoft pseudopotentials to the projector augmented-wave method, *Phys. Rev. B* 59 (1999) 1758, <https://doi.org/10.1103/PhysRevB.59.1758>.
- [93] S. Grimme, J. Antony, S. Ehrlich, H. Krieg, A consistent and accurate ab initio parametrization of density functional dispersion correction (DFT-D) for the 94 elements H-Pu, *J. Chem. Phys.* 132 (2010) 154104, <https://doi.org/10.1063/1.3382344>.
- [94] S. Grimme, S. Ehrlich, L. Goerigk, Effect of the damping function in dispersion corrected density functional theory, *J. Comput. Chem.* 32 (2011) 1456–1465, <https://doi.org/10.1002/JCC.21759>.
- [95] P. Trucano, R. Chen, Structure of graphite by neutron diffraction, *Nature* 258 (1975) 136–137, <https://doi.org/10.1038/258136a0>.
- [96] K. Mathew, V.S.C. Kolluru, S. Mula, S.N. Steinmann, R.G. Hennig, Implicit self-consistent electrolyte model in plane-wave density-functional theory, *J. Chem. Phys.* 151 (2019) 234101, <https://doi.org/10.1063/1.5132354>.
- [97] K. Mathew, R. Sundararaman, G. Letchworth-Weaver, T.A. Arias, R.G. Hennig, Implicit solvation model for density-functional study of nanocrystal surfaces and reaction pathways, *J. Chem. Phys.* 140 (2014) 084106, <https://doi.org/10.1063/1.4865107>.
- [98] J.A. Gauthier, S. Ringe, C.F. Dickens, A.J. Garza, A.T. Bell, M. Head-Gordon, J. K. Nørskov, K. Chan, Challenges in modeling electrochemical reaction energetics with polarizable continuum models, *ACS Catal.* 9 (2019) 920–931, <https://doi.org/10.1021/ACSCATAL.8B02793/>.
- [99] R. Rozada, J.I. Paredes, S. Villar-Rodil, A. Martínez-Alonso, J.M.D. Tascón, Towards full repair of defects in reduced graphene oxide films by two-step graphitization, *Nano Res.* 6 (2013) 216–233, <https://doi.org/10.1007/S12274-013-0298-6>.
- [100] P.-G. Ren, D.-X. Yan, X. Ji, T. Chen, Z.-M. Li, Temperature dependence of graphene oxide reduced by hydrazine hydrate, *Nanotechnology* 22 (2010) 055705, <https://doi.org/10.1088/0957-4484/22/5/055705>.
- [101] D.F. Carrasco, J.I. Paredes, S. Villar-Rodil, F. Suárez-García, A. Martínez-Alonso, J.M.D. Tascón, An electrochemical route to holey graphene nanosheets for charge storage applications, *Carbon* 195 (2022) 57–68, <https://doi.org/10.1016/J.CARBON.2022.04.003>.
- [102] M. Ayán-Varela, J.I. Paredes, S. Villar-Rodil, R. Rozada, A. Martínez-Alonso, J.M.D. Tascón, A quantitative analysis of the dispersion behavior of reduced graphene oxide in solvents, *Carbon* 75 (2014) 390–400, <https://doi.org/10.1016/j.carbon.2014.04.018>.
- [103] J.M. Munuera, J.I. Paredes, S. Villar-Rodil, A. Martínez-Alonso, J.M.D. Tascón, A simple strategy to improve the yield of graphene nanosheets in the anodic exfoliation of graphite foil, *Carbon* 115 (2017) 625–628, <https://doi.org/10.1016/J.CARBON.2017.01.038>.
- [104] J.T. King, A. Shakya, Phase separation of DNA: from past to present, *Biophys. J.* 120 (2021) 1139–1149, <https://doi.org/10.1016/J.BPJ.2021.01.033>.
- [105] A. Shakya, S. Park, N. Rana, J.T. King, Liquid-liquid phase separation of histone proteins in cells: role in chromatin organization, *Biophys. J.* 118 (2020) 753–764, <https://doi.org/10.1016/J.BPJ.2019.12.022>.
- [106] J. Winsberg, C. Stolze, A. Schwenke, S. Muench, M.D. Hager, U.S. Schubert, Aqueous 2,2,6,6-Tetramethylpiperidine-N-oxyl Catholytes for a high-capacity and high current density oxygen-insensitive hybrid-flow battery, *ACS Energy Lett.* 2 (2017) 411–416, <https://doi.org/10.1021/ACSENERGYLETT.6B00655>.
- [107] M. Ayán-Varela, Ó. Pérez-Vidal, J.I. Paredes, J.M. Munuera, S. Villar-Rodil, M. Díaz-González, C. Fernández-Sánchez, V.S. Silva, M. Cicuéndez, M. Vila, A. Martínez-Alonso, J.M.D. Tascón, Aqueous exfoliation of transition metal dichalcogenides assisted by DNA/RNA nucleotides: catalytically active and biocompatible nanosheets stabilized by acid-base interactions, *ACS Appl. Mater. Interfaces* 9 (2017) 2835–2845, <https://doi.org/10.1021/ACSAMI.6B13619>.
- [108] J.I. Paredes, S. Villar-Rodil, A. Martínez-Alonso, J.M.D. Tascón, Graphene oxide dispersions in organic solvents, *Langmuir* 24 (2008) 10560–10564, <https://doi.org/10.1021/LA801744A>.
- [109] S. Wang, B. Ru, H. Lin, Z. Luo, Degradation mechanism of monosaccharides and xylan under pyrolytic conditions with theoretic modeling on the energy profiles, *Bioresour. Technol.* 143 (2013) 378–383, <https://doi.org/10.1016/J.BIORTECH.2013.06.026>.
- [110] J. Masłowska, M. Malicka, Thermal behaviour of riboflavin, *J. Therm. Anal. Cal.* 3 (1988) 3–9, <https://doi.org/10.1007/BF01913365>.
- [111] H. Szatylowicz, O.A. Stasyuk, M. Solà, T.M. Krygowski, Aromaticity of nucleic acid bases, *WIREs Comput. Mol. Sci.* 11 (2021) e1509, <https://doi.org/10.1002/WCMS.1509>.
- [112] F. Glöckhofer, T.L.R. Bennett, A.V. Marsh, J.M. Turner, F. Plasser, M. Heeney, Functionalisation of conjugated macrocycles with type I and II concealed antiaromaticity via cross-coupling reactions functionalisation of conjugated macrocycles with type I and II concealed antiaromaticity via cross-coupling reactions, *Mol. Syst. Des. Eng.* 8 (2023) 713, <https://doi.org/10.1039/d3me00045a>.
- [113] D. Bahamon, M. Khalil, A. Belabbes, Y. Alwahedi, L.F. Vega, K. Polychronopoulou, A DFT study of the adsorption energy and electronic interactions of the SO<sub>2</sub> molecule on a CoP hydrotrating catalyst, *RSC Adv.* 11 (2021) 2947–2957, <https://doi.org/10.1039/c9ra10634k>.
- [114] D. Farmanzadeh, S. Ghazanfary, The effect of electric field on the interaction of glycine with (6,0) single-walled boron nitride nanotubes, *J. Serb. Chem. Soc.* 78 (2013) 75–83, <https://doi.org/10.2298/JSC120419046F>.
- [115] A. Zdzianuski, I. Ignatjev, T. Charkova, M. Talaikis, A. Lukša, A. Šetkus, G. Niaura, Shell-isolated nanoparticle-enhanced Raman spectroscopy for probing riboflavin on graphene, *Materials* 15 (2022) 1636, <https://doi.org/10.3390/MA15051636>.
- [116] P. Hu, Y. Song, L. Chen, S. Chen, Electrochemical activity of alkyne-functionalized AgAu alloy nanoparticles for oxygen reduction in alkaline media, *Nanoscale* 7 (2015) 9627–9636, <https://doi.org/10.1039/C5NR01376C>.
- [117] K.-H. Wu, D.-W. Wang, X. Zong, B. Zhang, Y. Liu, I.R. Gentle, D.-S. Su, Functions in cooperation for enhanced oxygen reduction reaction: the independent roles of oxygen and nitrogen sites in metal-free nanocarbon and their functional synergy, *J. Mater. Chem. A* 5 (2017) 3239–3248, <https://doi.org/10.1039/C6TA10336G>.
- [118] S. Fletcher, Tafel slopes from first principles, *J. Solid State Electrochem.* 13 (2009) 537–549, <https://doi.org/10.1007/S10008-008-0670-8>.
- [119] C.D. Jaimes-Paez, E. Morallón, D. Cazorla-Amorós, Few layers graphene-based electrocatalysts for ORR synthesized by electrochemical exfoliation methods, *Energy* 278 (2023) 127888, <https://doi.org/10.1016/J.ENERGY.2023.127888>.
- [120] L. Bouleau, S. Pérez-Rodríguez, J. Quilez-Bermejo, M.T. Izquierdo, F. Xu, V. Fierro, A. Celzard, Best practices for ORR performance evaluation of metal-free porous carbon electrocatalysts, *Carbon* 189 (2022) 349–361, <https://doi.org/10.1016/J.CARBON.2021.12.078>.
- [121] F.S. Gittleston, R.C. Sekol, G. Dubeck, M. Linardi, A.D. Taylor, Catalyst and electrolyte synergy in Li–O<sub>2</sub> batteries, *Phys. Chem. Chem. Phys.* 16 (2014) 3230–3237, <https://doi.org/10.1039/C3CP54555E>.
- [122] A. Vazhayil, L. Vazhayal, J. Thomas, S. Ashok, N. Thomas, A comprehensive review on the recent developments in transition metal-based electrocatalysts for oxygen evolution reaction, *Appl. Surf. Sci. Adv.* 6 (2021) 100184, <https://doi.org/10.1016/j.apsadv.2021.100184>.
- [123] J. Zhu, L. Hu, P. Zhao, L.Y.S. Lee, K.-Y. Wong, Recent advances in electrocatalytic hydrogen evolution using nanoparticles, *Chem. Rev.* 120 (2020) 851–918, <https://doi.org/10.1021/ACS.CHEMREV.9B00248>.
- [124] N. Karthik, T.N.J.I. Edison, R. Atchudan, D. Xiong, Y.R. Lee, Electro-synthesis of sulfur doped nickel cobalt layered double hydroxide for electrocatalytic hydrogen evolution reaction and supercapacitor applications, *J. Electroanal. Chem.* 833 (2019) 105–112, <https://doi.org/10.1016/J.JELECHEM.2018.11.028>.
- [125] C. Alex, S.C. Sarma, S.C. Peter, N.S. John, Competing effect of Co<sup>3+</sup> reducibility and oxygen-deficient defects toward high oxygen evolution activity in Co<sub>3</sub>O<sub>4</sub> Systems in Alkaline Medium, *ACS Appl. Energy Mater.* 3 (2020) 5439–5447, <https://doi.org/10.1021/ACSAEM.0C00297>.
- [126] C. Yüksel Alpaydın, S.K. Güllbay, C.O. Colpan, A review on the catalysts used for hydrogen production from ammonia borane, *Int. J. Hydrog. Energy* 45 (2020) 3414–3434, <https://doi.org/10.1016/J.IJHYDENE.2019.02.181>.
- [127] M. Gholinejad, M. Afrasi, C. Najera, Caffeine gold complex supported on magnetic nanoparticles as a green and high turnover frequency catalyst for room temperature A3 coupling reaction in water, *Appl. Organomet. Chem.* 33 (2019) e4760, <https://doi.org/10.1002/AOC.4760>.
- [128] H. Su, X. Zhao, W. Cheng, H. Zhang, Y. Li, W. Zhou, M. Liu, Q. Liu, Hetero-N-coordinated co single sites with high turnover frequency for efficient electrocatalytic oxygen evolution in an acidic medium, *ACS Energy Lett.* 4 (2019) 1816–1822, <https://doi.org/10.1021/ACSENERGYLETT.9B01129>.
- [129] H. Yu, B. Zhang, C. Bulin, R. Li, R. Xing, High-efficient synthesis of graphene oxide based on improved Hummers method, *Sci. Rep.* 6 (2016) 36143, <https://doi.org/10.1038/srep36143>.
- [130] C. Guo, Y. Cai, H. Zhao, D. Wang, Y. Hou, J. Lv, H. Qu, D. Dai, X. Cai, J. Lu, J. Cai, Efficient synthesis of graphene oxide by Hummers method assisted with an electric field, *Mater. Res. Express* 6 (2019) 055602, <https://doi.org/10.1088/2053-1591/AB023D>.

- [131] Q. Zhang, Y. Yang, H. Fan, L. Feng, G. Wen, L.-C. Qin, Synthesis of graphene oxide using boric acid in Hummers method, *Colloids Surf. A Physicochem. Eng. Asp.* 652 (2022) 129802, <https://doi.org/10.1016/j.colsurfa.2022.129802>.
- [132] N.I. Kovtyukhova, P.J. Ollivier, B.R. Martin, T.E. Mallouk, E.V. Buzaneva, A. D. Gorchinskiy, Layer-by-layer assembly of ultrathin composite Films from Micron-sized graphite oxide sheets and Polycations, *Chem. Mater.* 11 (1999) 771–778, <https://doi.org/10.1021/CM981085U>.
- [133] W.S. Hummers, R.E. Offeman, Preparation of graphitic oxide, *J. Am. Chem. Soc.* 80 (1958) 1339, <https://doi.org/10.1021/JA01539A017>.